UNIVERSITY *of York*

This is a repository copy of *Single-molecule and super-resolved imaging deciphers membrane behaviour of onco-immunogenic CCR5*.

Version: Accepted Version

Title

Single-molecule and super-resolved imaging deciphers membrane behaviour of onco-immunogenic CCR5

Authors

Patrick Hunter[1], Alex L. Payne-Dwyer[1,2], Michael Shaw[3,4], Nathalie Signoret[5] and Mark C. Leake[1,2,6],*

[1]Department of Biology, University of York, YO10 5DD, UK

[2]School of Physics, Engineering and Technology, University of York, YO10 5DD, UK

[3]National Physical Laboratory, Hampton Road, Teddington, Middlesex, TW11 0LW

[4]Department of Computer Science, University College London, London, WC1E 6EA, UK

[5]Hull York Medical School, University of York, YO10 5DD, UK

[6]Lead contact

*Correspondence: mark.leake@york.ac.uk

Summary

The ability of tumors to establish a pro-tumorigenic microenvironment is an important point of investigation in the search for new therapeutics. Tumors form microenvironments in part by the "education" of immune cells attracted via chemotactic axes such as that of CCR5-CCL5. Further, CCR5 upregulation by cancer cells, coupled with its association with pro-tumorigenic features such as drug-resistance and metastasis, has suggested CCR5 as a therapeutic target. However, with several conformational "pools" being reported, phenotypic investigations must be capable of unveiling conformational heterogeneity. Addressing this challenge, we performed super-resolution structured illumination microscopy (SIM) and single molecule partially TIRF coupled HILO (PaTCH) microscopy of CCR5 in fixed cells. SIM data revealed a non-random spatial distribution of CCR5 assemblies, whilst Intensity-tracking of CCR5 assemblies from PaTCH images indicated dimeric sub-units independent of CCL5 perturbation. These biophysical methods can provide important insights into the structure and function of onco-immunogenic receptors and many other biomolecules.

Introduction

The mechanism by which cancer cells obtain immune evasive features remains an open question. However, current research indicates that cancer cells are able to

manipulate chemokine networks to support tumor progression, with the main chemotactic axis utilised being that of C-C chemokine receptor type 5 (CCR5) and its ligand C-C chemokine ligand type 5 (CCL5) [1–3]. CCR5 is a member of the seven transmembrane family of G protein coupled receptors (GPCRs) and is found in various white blood cells including T-cells and macrophages. CCR5 responds to a range of chemokines, such as CCL5, known to induce chemotaxis towards sites of immune response [4]. Despite this immunogenic feature of the CCR5-CCL5 axis, cancer cells are capable of "educating" migrating immune cells to form an immunosuppressive tumor microenvironment [5–7]. Further, oncogenic transformation of cells has been shown to increase the surface expression of CCR5 (Erreni et al., 2009; Mañes et al., 2003; Sales et al., 2014; Vaday et al., 2006). As a result, CCR5 has become a strong point of investigation in studies relating to both immunology and cancer.

Studies have linked the upregulation of CCR5 by cancer cells with poor prognosis for patients, with the CCR5-CCL5 axis being found to aid in tumor growth, metastasis and drug-resistance amongst other pro-tumorigenic features [8–10]. These investigations have culminated in the consideration of the CCR5-targeted drug Maraviroc, previously utilised as a therapeutic for HIV, to be repurposed as a clinical treatment for cancer patients [1,11,12]. It is clear that the CCR5-CCL5 axis plays an important role in both immune dynamics and tumor progression, and that investigations into the behavior of CCR5 along the surface membrane are likely to be beneficial in the development of new therapeutics.

Previous studies investigating the antigenic behaviour of CCR5 suggest the existence of multiple conformational subpopulations of CCR5, an observation that is derived from the characteristic recognition of structurally distinct ligands by varying proportions of cell surface CCR5 [13–16]. Further, CCR5 has been shown to exist in both homodimeric and heterodimeric states, with the homodimerization of CCR5 being shown to take place in the endoplasmic reticulum before reaching the cell surface [17], any downstream clustering would therefore be expected to carry a periodicity in apparent stoichiometry of two molecules [18]. Considering that the various purported conformational and oligomeric states of CCR5 exhibit downstream effects on the receptor chemotactic functionality [14,19], the nature of this heterogeneity requires further investigation.

Although earlier single-molecule studies have been carried out using GPCRs [20–22], previous investigations into the oligomeric status of CCR5 in particular have been focused within the bulk ensemble regime, utilising techniques such as standard fluorescence confocal microscopy, flow cytometry and Western blotting [15,17]. Through the extension of cell-surface CCR5 investigations to include 3D super-resolution microscopy and high-speed single-molecule tracking, here we have been able to visualise CCR5 expression with a spatial resolution twice that of the optical diffraction limit as well as provide stoichiometry estimates based on single-molecule measurements, thereby unveiling the heterogeneity lost by bulk ensemble techniques. Further, studying the effects of ligand perturbations make it possible to draw additional conclusions regarding the effects of CCL5 binding on the cell surface expression of CCR5.

Here, we introduce a study which utilises the accompaniment of two light microscopy techniques, chosen for their high spatial and temporal resolution, to study Chinese hamster ovary (CHO) cell lines which have undergone genetic modification for the production of CCR5 in the absence of endogenously produced CCR5. Our study employs structured illumination microscopy (SIM) for the investigation of cell surface CCR5 distributions within CHO-CCR5 cells, a cell line utilised in multiple previous studies [23–26]. Also, through the creation of a new line of transfected CHO cells, which express CCR5 N-terminally fused to GFP to a level compatible with single-molecule microscopy, it has been possible to provide single-molecule stoichiometry estimates using a newly developed microscopy technique that combines the high signal-to-noise ratio of total internal reflection fluorescence (TIRF) microscopy whilst benefiting from the increased penetration depth of Highly Inclined and Laminated Optical sheet (HILO) microscopy [27]. This new imaging mode, that we denote Partially TIRF coupled HILO (PaTCH) microscopy is distinguished from TIRF and HILO through the employment of an optimised angle of incidence which aims to improve the study of transmembrane proteins in cells exhibiting a complex basal membrane topology. TIRF relies on an angle of incidence which surpasses the critical angle of a glass-water interface, ensuring total internal reflection of the excitation beam at the coverslip and thereby resulting in an exponentially decaying evanescent field that extends a short distance through the sample. This evanescent field allows for the signal enhancement of molecules only within a few hundred nanometers of the coverslip surface whilst reducing intracellular background. Conversely, HILO employs a lower angle of incidence which results in the transmission of the excitation beam through the sample at a specified angle, reducing the excitation of out-of-focus layers and back-scattered light, and is therefore typically used for intracellular imaging with lower background albeit without benefiting from any signal enhancement. By employing an intermediate angle, PaTCH aims to produce an excitation field that is coupled jointly into TIRF and HILO modes, thereby providing an increased signal from molecules within the basal membrane when compared with HILO whilst allowing for the excitation of molecules above the limited excitation field achieved by TIRF (see Figure S1). Finally, using this new technique we then demonstrate how these methods can be used to investigate the surface expression and aggregation of CCR5 after exposure to the receptor's CCL5 ligand.

Results

SIM reveals CCR5 as distinct puncta distributed throughout the cell membrane in 3D

Initial investigations aimed to visualise the distribution of CCR5 in CHO-CCR5 cells, for which previous bulk ensemble studies had been performed. For this purpose, SIM was used to acquire super-resolution images of CHO-CCR5 labeled with the CCR5 mAb MC-5, itself labeled with DyLight 650 (Figure 1 a-g). Representation of these images included the correction of photobleaching effects on the fluorescence intensity, the exclusion of background fluorescence located outside the cell, as well as the inclusion of magnified insets of the CCR5 puncta. From these images we see that

membrane-bound CCR5 assemblies appear as distinct puncta throughout the entire plasma membrane, with puncta appearing uniformly distributed along the basal membrane. Further, due to the external labelling of CCR5, in cross-sectional images corresponding to planes above the basal membrane puncta are only visible within annulus-shaped regions of the cell surface.

Despite the increase in background fluorescence seen in Figure 1 g) due to photobleaching correction, the annular distribution of fluorescent foci is clearly retained. Finally, acquisition of optically sectioned slices allowed the reconstruction of color depth projections, as well as 3D images and videos, as shown in Figure 1 h, i) and Video S1. These reconstructions enable the visualisation of this annular distribution of cell surface CCR5, thereby revealing the topology of the cellular exterior while further highlighting the uniformity of the CCR5 distribution.

Clustering behavior of CCR5 assemblies is revealed through Ripley's H function-based analysis

Mammalian cells present a variety of cell morphologies, including membrane protrusions which can be caused by a stress response to sample preparation. Although these filopodia are not of high biological relevance to this investigation, the extensions of the representative cell shown in Figure 2 a-d) provide a clear illustration of the increased image quality (higher spatial resolution and image contrast) of SIM over traditional widefield microscopy. This improved image quality, coupled with the optical sectioning property of SIM, aid quantitative analysis of image data and enable puncta of CCR5 assemblies to be isolated from the cellular background through intensity thresholding, as shown in Figure 2 c). Closer investigation of these isolated puncta reveals a spatial distribution with distinct "hot spots" as shown in Figure 2 d). These results indicate the existence of spatial clustering of individual puncta. To analyse this further, we performed clustering analysis using Ripley's H function [28] on the centroids of isolated clusters. As represented in Figure 2 e), this method is based on the counting of objects at increasing distance averaged over all possible origin points inside the cell, and can be used to describe the level of clustering, uniformity or dispersion of points. By visualising the Ripley's H values as a function of radius spanning the diameter of the cell's basal membrane, we see that net clustering of points is characterised by accumulation of positive Ripley's H values across the cell, as shown in Figure 2 f-g). The modal clustering gradient thereby provides an estimation of the spatial correlation of CCR5 puncta throughout the cell, with the modal average gradient of CHO-CCR5 cells found to be positive: $dH(r)/dr$ = 0.004 ± 0.001. The initial minima displayed in the Ripley's H value distribution provides an estimate for the nearest neighbor distance between CCR5 puncta, with the average for CHO-CCR5 cells measured at 290 ± 10 nm.

Clones of GFP-CCR5 CHO cells developed for PaTCH microscopy and characterised using flow cytometry

To determine structural characteristics of the CCR5 assemblies, we performed single-molecule PaTCH microscopy-based studies to measure the number of molecules present in assemblies, which we denote as the stoichiometry. While PaTCH benefits from the simplicity of constitutively fluorescent probes and does not require

photoswitchable or photoactivatable probes [29,30], the successful investigation of individual CCR5 assemblies using PaTCH microscopy does rely on fluorescent proteins being expressed to a level compatible with single-molecule localization microscopy. For this purpose, CHO cells transfected to express GFP-CCR5 fusion proteins underwent single-cell cloning to create several populations with varying levels of expression. Figure 3 shows one such population, optimised for single-molecule imaging. In Figure 3 a-c) we see that despite exhibiting low expression suitable for single-molecule studies, the GFP expression of the positive sample is significantly higher than that of the control in both flow cytometry and microscopy-based experiments, providing confidence in this new model for CCR5 investigations. Additionally, to confirm the functionality of CCR5 in this newly created cell line, we performed a calcium flux assay (see Figure S2 a). These results reveal CCL5-induced calcium mobilisation in agreement with previous studies [31], albeit at a level that is representative of the lower CCR5 expression exhibited by this cell line.

PaTCH investigation of basal membrane GFP-CCR5 also reveals CCR5 assemblies as small puncta

As can be seen in Figure 4 a), despite a reduction in expression, GFP-CCR5 forms distinct puncta across the basal membrane of transfected CHO cells in a qualitatively similar distribution to that of DyLight 650-MC-5 labeled CCR5 in CHO-CCR5 cells, as shown in Figure 4 b). Althoug the increased spatial resolution of SIM images provides improved segmentation of CCR5 puncta for the determination of spatial clustering, high-speed PaTCH microscopy allows the determination of time-dependent processes such as dye photobleaching effects. Although further studies are required into the accurate determination of puncta diameter in both respective cell models, the general uniformity in the size of CCR5 puncta between both cell models provides confidence that any spatial dependence in CCR5 expression between these two models is related.

Stoichiometry measurements reveal CCR5 assemblies to comprise homodimers

Utilising the single-molecule sensitivity of PaTCH microscopy, we are able to identify the characteristic brightness of a single GFP as the modal intensity of single GFP-CCR5 molecules following sufficient photobleaching, further confirmed using recombinant GFP and the quantification of single-molecule photobleaching steps in fluorescence intensity (see Figure S3 b). This global value is used to normalise the initial intensity of GFP-CCR5 foci in order to acquire estimates of stoichiometry. A wide distribution of stoichiometries is revealed by collating all detected tracks across all GFP-CCR5 CHO cells (represented as a kernel density estimate [32] in Figure 5). This population of independent track-derived stoichiometries shows characteristic peaks, with the average nearest-neighbor interval between independent stoichiometry measurements revealing the typical periodicity inside oligomeric assemblies, if such periodicity exists [33]. Although the accurate measurement of small differences between two large stoichiometries is difficult, it is possible to successfully average those differences over many pairs (see Methods: Single particle tracking). Thereby, for CCR5 in the absence of ligand, we find the average periodicity to be 2.3 ± 0.5 CCR5

molecules (Figure 5 inset), indicating a strong tendency for CCR5 molecules to occur in dimeric subunits inside CCR5 assemblies.

Tracking of single molecules in PaTCH after addition of CCL5 indicates a broader spread of CCR5 foci stoichiometries

This study was extended by applying the above methods to study CCR5 upon stimulation with the agonist CCL5 at a concentration of 100 nM. CHO-CCR5 cells treated for 5 minutes with CCL5 were imaged using SIM microscopy as shown in Figure 6 a-i). As in Figure 1, representation of these images included the correction of photobleaching, the exclusion of background fluorescence located outside of the cell and the inclusion of magnified insets of the CCR5 puncta. However, this cell is displayed using slightly differing contrast settings to enable optimal image presentation, despite small qualitative differences in brightness between cells (see Figure S4). In a similar manner to Figure 1, we see the expression of CCR5 assemblies as small puncta throughout the cell membrane, with CCR5 uniformly distributed across the basal membrane and visible within approximately annulus-shaped regions for imaging planes above the basal membrane, as visualised in 3D (see Video S2).

The interaction between CCR5 and CCL5 is a process reported to induce internalisation, with CCL5 perturbed cells being expected to exhibit a reduction in cell surface CCR5. Despite this, the SIM image data do not indicate any reduction in the overall number of puncta in perturbed versus non-perturbed cells. The PaTCH images provide quantitative detail which confirms that addition of CCL5 does not tend to change the average number of CCR5 assemblies, as the mean number of tracks we detect are not significantly different before and after CCL5 (46.1 ± 4.8 and 51.1 ± 6.8 tracks per cell respectively) under the Brunner-Munzel (BM) test (n=18, p=0.429 | not significant at adjusted p<0.01 level, NS). The mean stoichiometry of these assemblies lies in the vicinity of ~20 molecules regardless of CCL5 addition (BM test: 17.1 ± 0.4 and 18.6 ± 0.5 molecules before and after CCL5 addition respectively, n=920, p=0.145 |NS). Taken together, these results suggest the total amount of CCR5 presented on the cell surface is approximately conserved under our experimental conditions.

However, CCL5 appears to affect large and small assemblies of CCR5 differently. We see a larger spread of stoichiometry of assemblies in perturbed cells (Figure 6 j-k) than can be accounted for by any difference in sampling variance. At the lower end, assemblies are more commonly comprised of approximately 8 CCR5 molecules, while at the higher end CCR5 contributes towards the growth of larger assemblies of greater than approximately 36 molecules. These two sub-groups are populated at the expense of intermediate assemblies near the mean stoichiometry. This is confirmed by the difference in the means of each, before and after CCL5 addition (BM test at stoichiometry < 15 molecules, n=436, p=0.0085|*; at stoichiometry > 15 molecules, n=480, p=0.0053|*), despite almost identical numbers of assemblies in each group.

By studying CCL5 perturbation in GFP-CCR5 CHO cells using PaTCH microscopy, we determined an average periodicity in stoichiometry of 2.2 ± 0.3 CCR5 molecules in the assemblies after perturbation. This is consistent with the result prior to ligand exposure (Figure 5 inset), and strongly indicates that the consistent dimeric

composition of CCR5 within assemblies is unaffected by CCL5 (see Figure S5). Additionally, the effect of extended ligand perturbation was investigated using a potent analog of CCL5 known as PSC-RANTES [13,34] at a concentration of 100 nM (see Figure S2 b). This flow cytometry-based assay monitored the accessibility of the chemokine binding site and the GFP moiety of GFP-CCR5 under varying duration of ligand exposure. This investigation revealed a reduction in both the accessibility of GFP and the epitope overlapping with the chemokine binding site, indicating ligand-binding and subsequent internalisation of GFP-CCR5. However, when compared with previous studies performed on CHO cells expressing wild-type CCR5 [23], GFP-CCR5 exhibits a slower internalisation response.

Discussion

In this study we have investigated the membrane behaviour of CCR5 expressed in fixed model cell lines using both structured illumination microscopy (SIM) and a new mode of imaging we have developed called Partially TIRF coupled HILO (PaTCH) microscopy. Using this combination of advanced biophysical techniques, we have been able to make observations into the clustering of membrane bound CCR5 as well as perform single-molecule investigations into the stoichiometry of these assemblies. Through the addition of perturbations employing the CCR5 agonist CCL5, we have been able to make preliminary observations into the ligand-dependent change in CCR5 behavior as proof-of-concept for the quantitative potential towards new biological insights with this approach.

SIM investigations of CCR5

Initial investigations into the distribution of CCR5 foci were carried out using an established line of GFP-CCR5 expressing CHO cells that have been utilised in preceding studies. Our study aimed to unveil the distribution of CCR5 using super-resolution SIM microscopy, thereby allowing the precise localization of CCR5 for the analysis of its clustering behavior. The resulting 3D image data, which captured DyLight 650-MC-5 labeled CCR5 assemblies from the basal to the apical membrane, revealed that CCR5 collects into small puncta throughout the entire plasma membrane. Through the localization of the intensity centroids of these puncta we were able to quantify the level of clustering in the CCR5 distribution using Ripley's H-function. Comparing these results with that of a randomly generated distribution of points, we found that CHO-CCR5 exhibits a clustered distribution with a modal clustering gradient of 0.004 ± 0.001. These results indicate that the puncta in which CCR5 appear to collect are in a non-random spatial distribution over the plasma membrane. Additional investigations are needed to determine whether the location of CCR5 puncta is correlated to a biological process and whether this organisation serves specific cellular roles. Finally, analysis of Ripley's H values over a short range facilitated the determination of the nearest neighbor separation of CCR5 puncta with the mean distance being 290 ± 10 nm, a result that further guides the characterisation of CCR5 expression.

PaTCH microscopy investigations of CCR5

To provide information on the structure of these CCR5 assemblies we performed single-molecule investigations using PaTCH microscopy. For this purpose, a new line of cells was created that stably expressed CCR5 at a level suitable for single-molecule microscopy. As well as low expression, this cell model required fluorescent labeling that could guarantee a ratio of one probe per CCR5 molecule for the purposes of molecular stoichiometry measurements. We therefore developed a line of CHO cells that stably express GFP-CCR5 and confirmed functionality and appropriate expression levels using flow cytometry-based calcium flux assays and immunolabeling. Utilising PaTCH microscopy to study this newly developed cell line, we were able to confirm the collection of CCR5 into small puncta and track the fluorescence intensity of these assemblies through time as they decayed due to photobleaching. Using this data and the method utilised in previous studies (Jin et al., 2021; Leake et al., 2006, 2008; Reyes-Lamothe et al., 2010; Syeda et al., 2019; Wollman et al., 2021, 2020b) we were able to determine the stoichiometries of individual CCR5 assemblies and form stoichiometry distributions for individual cell populations. We found that the distribution of CCR5 stoichiometries exhibits a significant range and can be characterised by the existence of periodic peaks in stoichiometry with an average interval of 2.3 ± 0.5 molecules. The existence of this periodicity leads us to believe that CCR5 puncta on the basal membrane likely consist of homodimeric sub-units, a result that is supported in the literature with other groups reporting the existence of dimeric CCR5 [17,18]. Recent studies have been conducted that similarly employ CCR5 fused with GFP expressed within CHO cells, providing validity to this method of reporting [41], however these studies employ GFP coupled on the C-terminus of CCR5, as distinct from the N-terminus coupling in our study. Due to the existence of a PDZ binding domain on the C-terminus of CCR5, C-terminal coupling raises potential concerns regarding the downstream effect of PDZ masking on the behavior of CCR5 [42,43].

Investigations of CCR5 after CCL5 interaction

Our investigations into the membrane behavior of CCR5 were extended through the perturbation of this model using the CCR5 agonist CCL5. This perturbation has been studied previously using bulk ensemble techniques which indicate progressive downmodulation of CCR5 [24]. Although our super-resolution SIM analysis did not detect a significant change in surface CCR5 following 5 minutes of ligand stimulation, we noted that the spread of stoichiometry values acquired through PaTCH analysis increased following stimulation, despite a similar level of overall tracked assemblies. The increase in frequency of both small and large stoichiometries, coupled with a decreased incidence of intermediate stoichiometries, could be associated with the movement of CCR5 subunits from their basal membrane location towards sites of internalisation. Through findings from previous investigations [23,44,45], these sites are suspected to be clathrin-coated pits in which CCR5 is theorised to report for the purposes of internalisation and recycling. Although a promising preliminary finding in our proof-of-concept study here, to provide further evidence for this model would sensibly require further single molecule investigation using varying levels of ligand perturbation. Through acquiring a dataset with varying perturbation times, one would aim to monitor further changes in the stoichiometry distribution coinciding with the

downstream receptor internalisation seen in bulk ensemble investigations (see Figure S2 b). Further, investigations including the fluorescent labeling of clathrin would provide insight into the colocalization of CCR5 and clathrin-coated pits.

Summary

Through the application of complementary biophysical techniques, we have been able to perform super-resolved, single-molecule precise investigations of chemokine receptor CCR5 expressed in model cell lines. These investigations have provided hitherto unreported super-resolution images of CCR5 that allow us to reveal higher-order clustering of CCR5 subpopulations. Therefore, with the heterogeneity of GPCR subpopulations being linked with their signaling function [46], the ability of these techniques to characterise different structures and behaviors within independent sub-populations will facilitate the production of results relevant to the fields of both immunology and immuno-oncology. By utilising the suitability of these microscopy techniques for the investigation of live-cell imaging, we will gain the ability to track receptors as they travel throughout the plasma membrane, thereby quantifying the dynamic characteristics of CCR5 assemblies. In addition, our investigations can be readily augmented to include additional perturbations of both CCL5 and other CCR5 agonists and antagonists, thereby allowing single-molecule studies into the effects of CCR5 targeted drugs, such as Maraviroc. Finally, although the study of CCR5 within model cell lines allows the measurement of CCR5-ligand characteristics in the absence of competing binding partners, future extensions of our study will aim to employ the use of primary onco-immunogenic cells for the investigation of endogenously expressed CCR5, thereby enabling examination into the effects of a natural plasma membrane environment on the behavior of CCR5.

Limitations of study

In this study, we employed fixed model cell lines transfected to express CCR5. Although these model cells allow us to study CCR5 and its agonist CCL5 in the absence of competing binding partners, the biological relevance of this model system is limited by the fact that these are not primary cells. By extending this study to the investigation of CCR5 expressed endogenously in primary onco-immunogenic cells, we can perform a rigorous study that accounts for the presence of other chemokine receptors and ligands. Although this study aims to mitigate against effects induced by sample preparation, the extension of this study to investigate live cells would further mitigate any effect on the CCR5 distribution and cell morphology induced through formalin fixation and mounting and would allow for the determination of unhindered receptor dynamics. Emerging single-molecule optical microscopy techniques of single-molecule light sheet and single-molecule light field [47] may prove valuable in the future to address questions of receptor dynamics and stoichiometry [48], by enabling potential visualisation of both apical and basal surfaces and 3D positions of single fluorophores to be determined from fast parallax measurements, respectively.

However, the extension of the methods discussed to the investigation of CCR5 within live tumor tissues introduces challenges associated with the imaging of optically thick

samples, potentially comprising multiple cell layers, and the unavailability of stable receptor expression. This extension presents the opportunity for further development of the employed microscopy techniques, such as PaTCH, that are currently capable of imaging only a thin layer above the optical substrate, thereby allowing the investigation of single molecules above the basal membrane. Additionally, this study sees the employment of fluorescent labels that require exposure to high levels of laser excitation intensity, thereby raising potential concerns regarding the permanent photobleaching of reporters and phototoxicity effects to the cells. Although photodamage issues are mitigated in our study through the use of fixed end-point based experiments, any future extension to live cells will require the consideration of potential cell damage if cells are to remain viable in culture. Finally, despite the successful use of GFP and DyLight 650 dye to determine single-molecule, super-resolved stoichiometry and spatial localization of CCR5 in our study, these dye probes do possess room for improvement. Despite the enduring popularity of GFP, fluorescent proteins are comparable in size to CCR5 and have low fluorescence intensity when compared with modern organic dyes. When comparing the ligand-induced internalisation of GFP-CCR5 with that of CCR5, as investigated in previous studies [23], we see a slower rate of internalisation that indicates a GFP-induced effect on receptor mobility. Through the introduction of SNAP-tag® or similar technologies into our cell model we may improve the overall signal-to-noise ratio of future acquisitions using small bright organic dyes that exhibit less perturbation to normal receptor function. Further, through the development of immunofluorescent labels that offer a dye to protein ratio of 1:1, we will be better equipped to perform measurements that report on the number of CCR5 molecules in distributions imaged using SIM.

Author contributions

Conceptualization: M.L, P.H, A.P-D, N.S

Project administration, Supervision and Funding Acquisition: M.L, N.S, M.S

Investigation, Methodology, Data curation, Analysis and Visualization: P.H, A.P-D, N.S, M.S

Software: A.P-D, P.H

Writing – original draft: P.H, A.P-D

Writing – review & editing: P.H, A.P-D, N.S, M.L, M.S

Acknowledgements

the UK's Department for Business, Energy and Industrial Strategy through the National Measurement System.

Declaration of interests

The authors declare no competing interests.

Inclusion and diversity

We support inclusive, diverse, and equitable conduct of research.
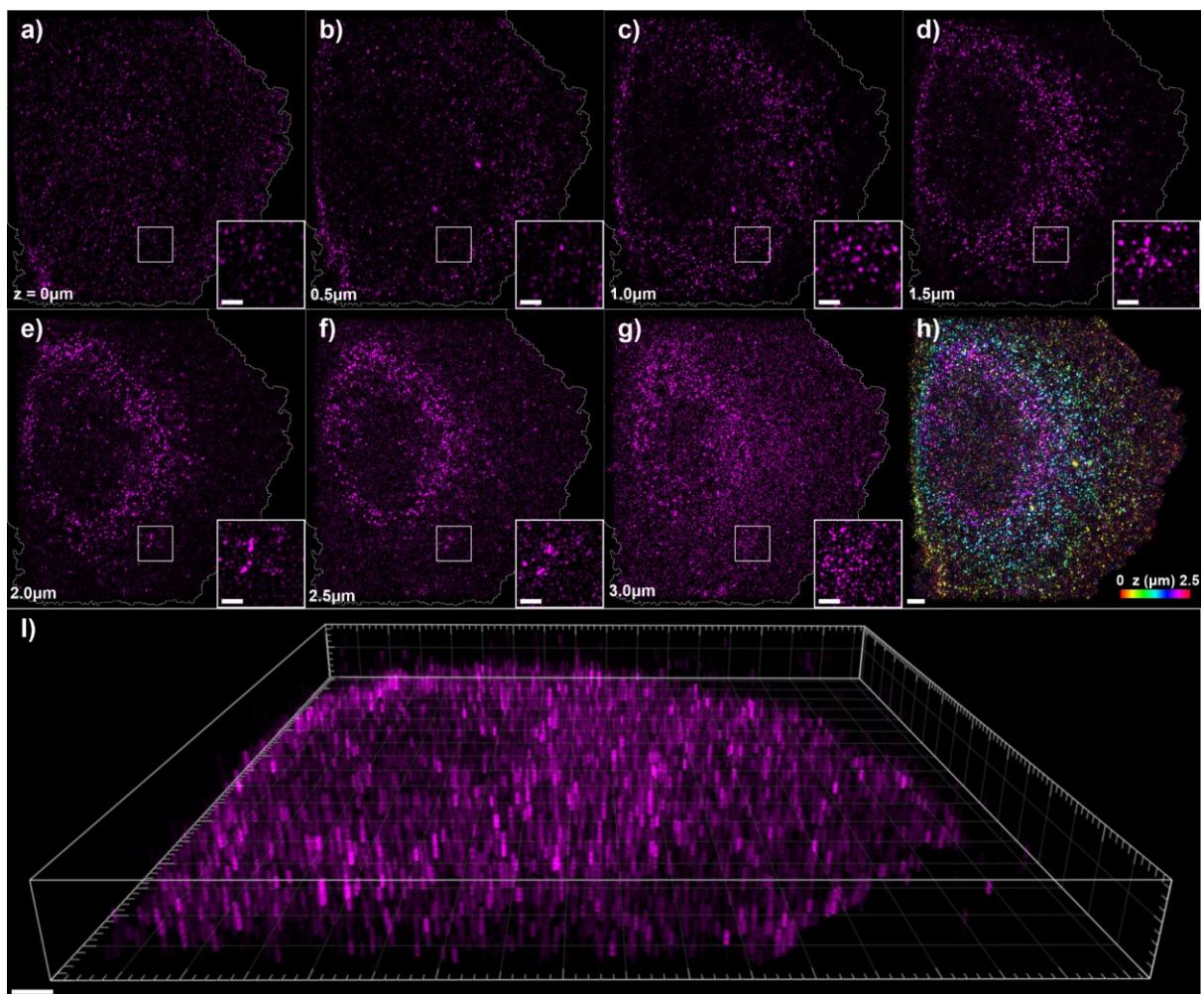
Figure titles and legends

Figure 1. SIM images of CHO-CCR5 cells labeled with DyLight 650-MC-5*. a - g) Individual SIM image planes of a CHO-CCR5 cell, from the basal membrane through to the apical membrane in 500 nm steps, displaying cell boundary segmentation and magnified insets. h) Color depth projection over the images shown in a-f). i) 3D reconstruction of cell images shown in a-g). (Scale bar 2 μm, (magnified insets 1 μm)).*
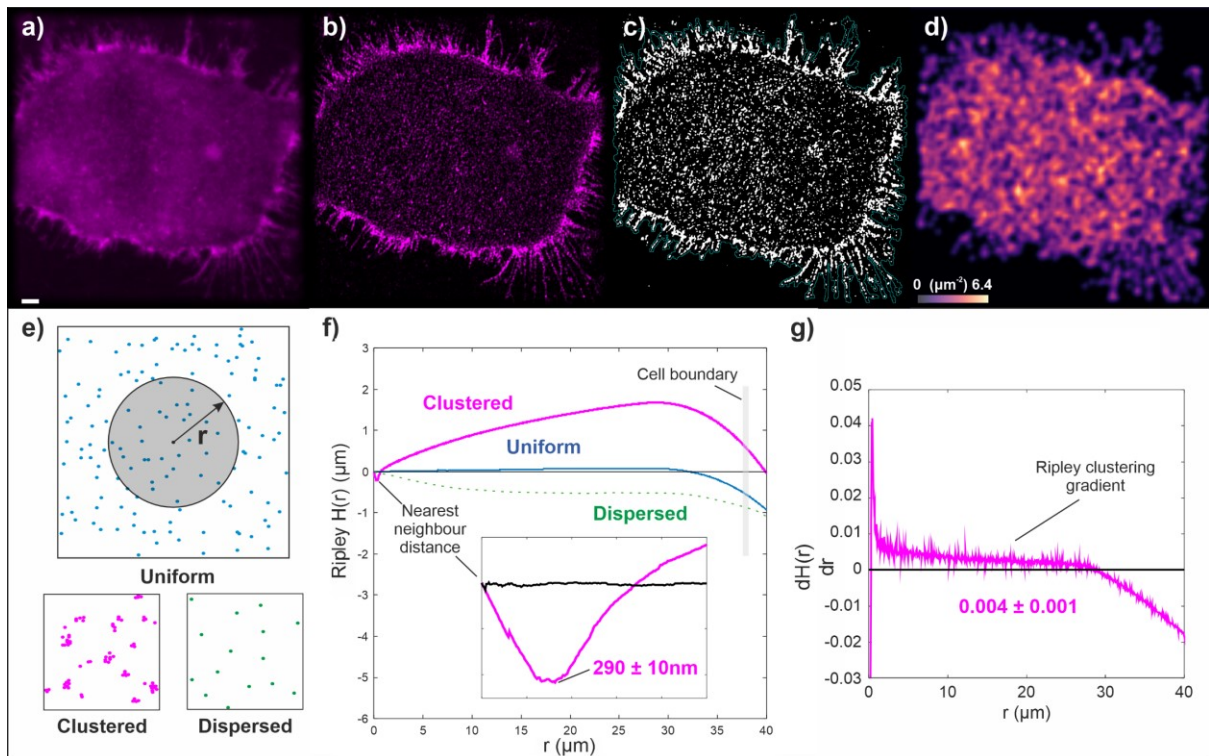
***Figure 2. Images and quantitative clustering metrics of CCR5 in the basal membrane of CHO-CCR5 cells labeled with DyLight 650-MC-5**. a) Widefield image of the basal membrane of a representative CHO-CCR5 cell (scale bar 2 μm). b) SIM reconstruction of the same cell. c) Binarized mask of the SIM image displaying thresholded CCR5 puncta. d) Number density distribution of individual puncta centroids, ranging from 0 - 6.4 μm⁻². e) Illustration demonstrating the function of Ripley's H analysis in the investigation of uniform, clustered and dispersed point distributions. f) Distribution of Ripley's H values for a real representative CHO-CCR5 cell (magenta) and a generated 2D map of points whose displacement separations are sampled from a random Poisson distribution (blue). Also shown is an illustrative curve depicting the expected results of a generic dispersed point distribution (green dotted). Inset shows the same distribution of Ripley's H values for the CHO-CCR5 cell (magenta) and random point distribution (blue) over a range of 0 - 1 μm and provides an average nearest-neighbor distance for binarized CHO-CCR5 puncta (N=10 cells). g) The gradient of the distribution of Ripley's H values for the CHO-CCR5 cell represented in f) which provides a modal average clustering gradient for CHO-CCR5 (N=10 cells).*
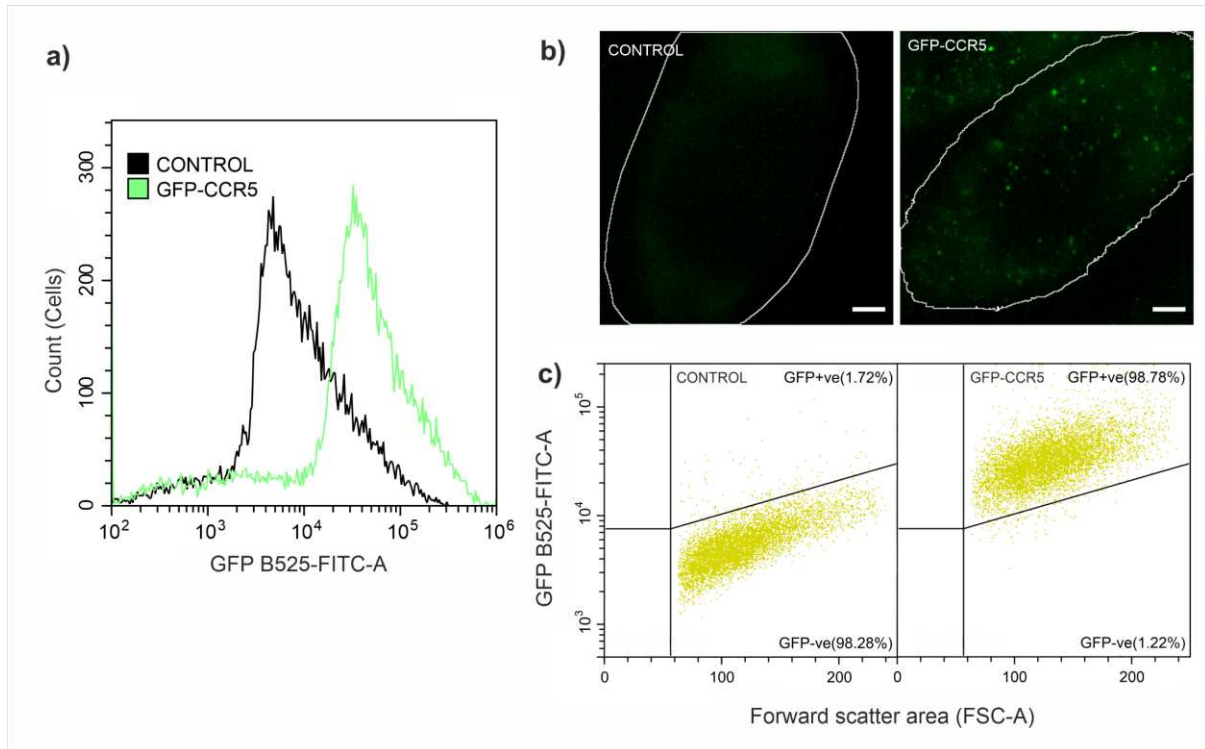
Figure 3. Characterisation of GFP-CCR5 expression in transfected CHO cells using flow cytometry and PaTCH microscopy confirms increase above control samples. *a) Distribution of GFP emission intensity over several hundred cells for both control and GFP-CCR5 positive samples. b) PaTCH images of the basal membrane of both control and GFP-CCR5 positive cells. Cell boundary segmentation shown in white. (Scale bar 2 µm). c) Scatterplot of GFP-range emission intensity against the forward scatter area of both control and GFP-CCR5 positive cells. Both a) and c) show cell populations after gating to remove debris and doublets. (See also Figure S2)*
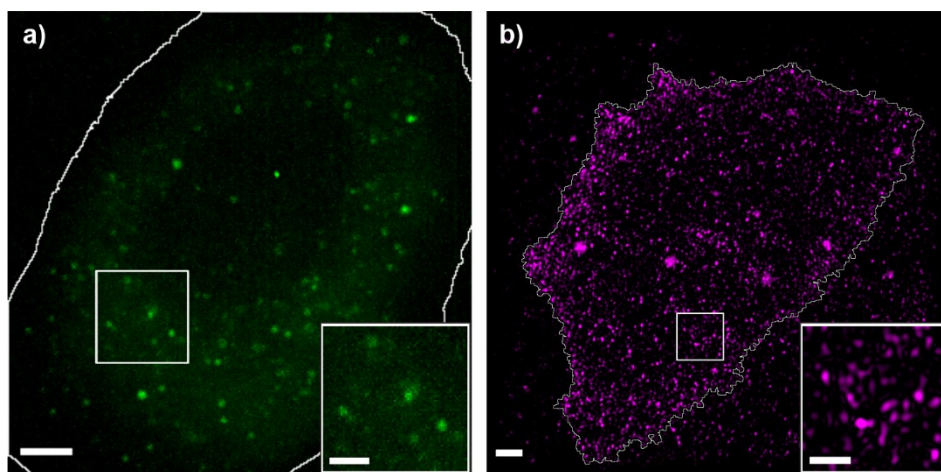

Figure 4. Comparison of GFP-CCR5 CHO cells with established CHO-CCR5 cells. Fluorescent labels shown to be distributed in distinct puncta across cellular membranes in a) GFP-CCR5 expressing CHO cells imaged using PaTCH microscopy and b) DyLight 650 labeled CHO-CCR5 cells imaged using SIM. Cell boundary
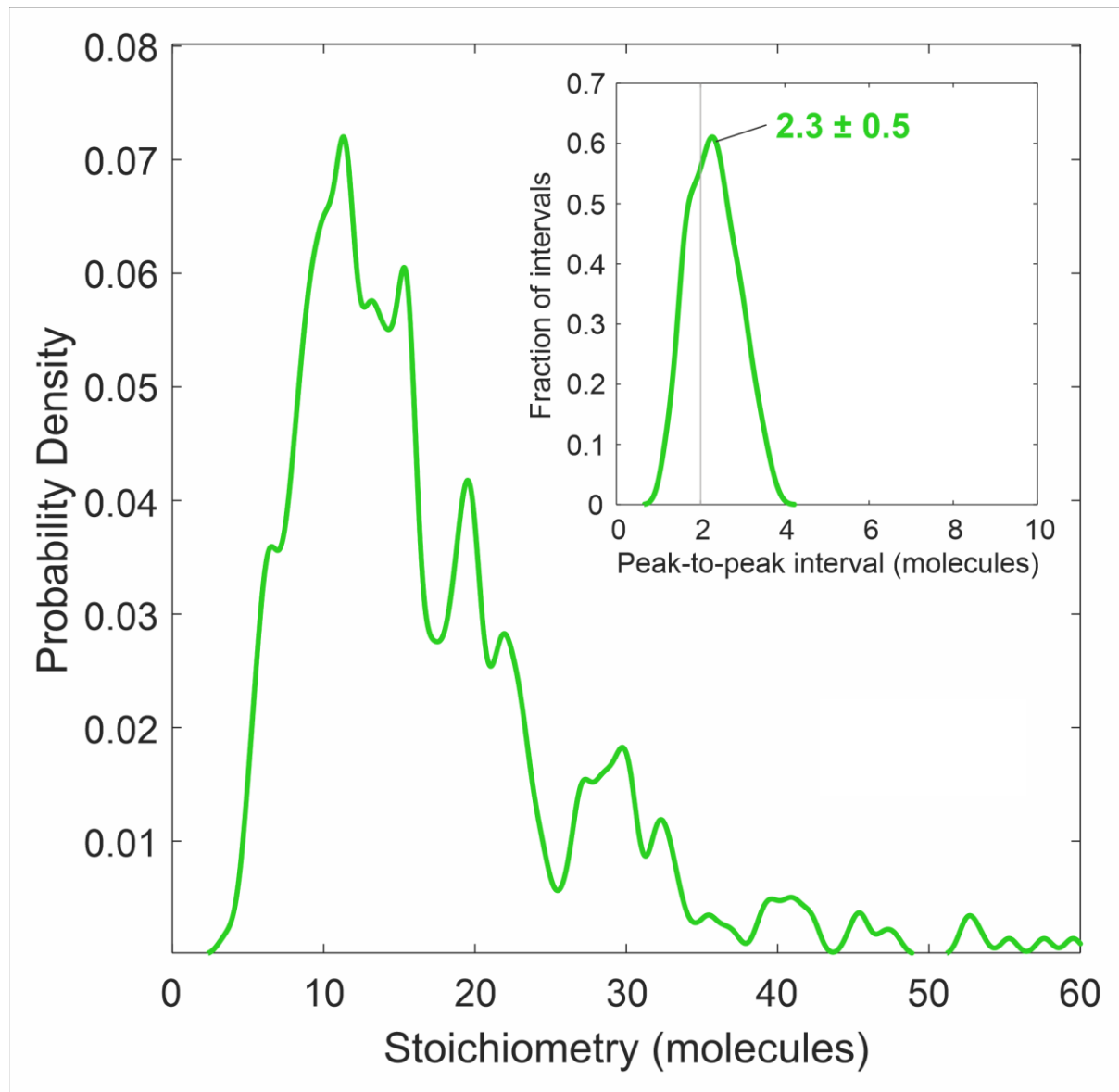
Figure 5. Periodic stoichiometry distribution indicates that CCR5 assemblies comprise dimeric subunits*. Kernel density estimates of stoichiometry and (inset) periodic stoichiometry intervals of GFP-CCR5 associated foci (N=460 tracks) detected by PaTCH microscopy in GFP-CCR5 transfected CHO cells (N=9 cells). Kernel width = 0.6 molecules, corresponding to the total uncertainty in the single molecule stoichiometry, rather than statistical fluctuations. Measured intervals in probability density or stoichiometry are therefore more reliable at lower stoichiometry. (See also Figure S3)*
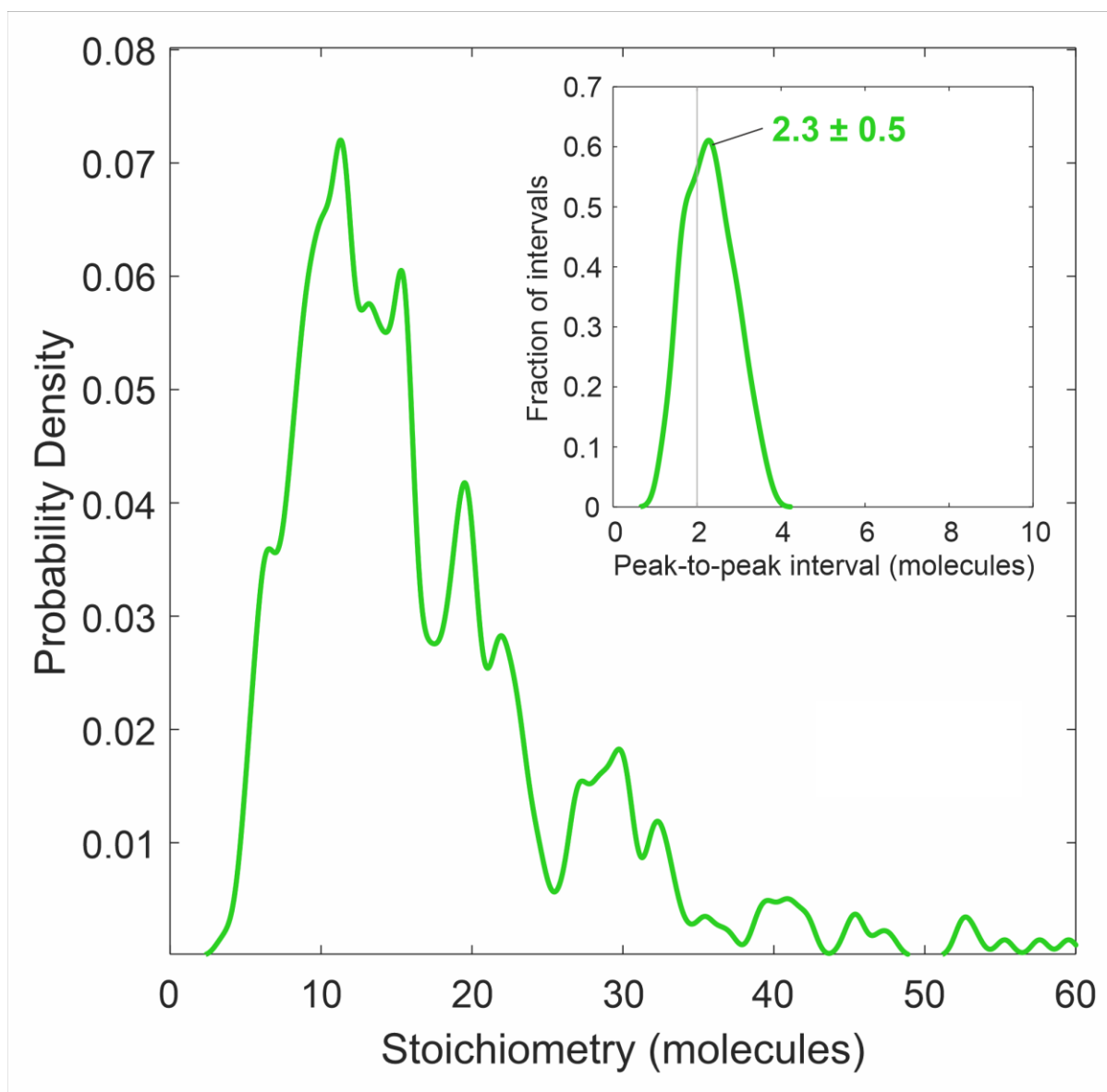
Figure 6. Investigating the perturbation of CCR5 with agonist CCL5 using SIM and PaTCH microscopy. *a - g) Individual SIM images of a CCL5 perturbed CHO-CCR5 cell, optically sectioned from the basal membrane through to the apical membrane in 500 nm increments, including cell boundary segmentation and magnified insets. h) Color depth projection of cell images shown in a -f). i) 3D reconstruction of cell images shown in a - g) (Scale bar 2 µm, (magnified insets 1 µm)). j) Numbers of GFP-CCR5 tracks detected per cell, with and without CCL5 perturbation, represented as dots spread horizontally to allow individual visualisation (N=9 or 11 cells, respectively). k) Violin distributions of the stoichiometry of GFP-CCR5 assemblies, with and without CCL5 perturbation, represented as dots spread horizontally to allow individual visualisation (N=460 or 507 tracks respectively). Bars, boxes and whiskers denote median, interquartile range (IQR) and 2.5× IQR respectively and the cross denotes the mean ± SEM for both j and k. (See also Figures S2, S4 and S5)*

STAR Methods

Resource availability

Lead contact

Further information and requests for resources and reagents should be directed to the lead contact, Mark C. Leake (mark.leake@york.ac.uk).

Materials availability

This study did not generate new unique reagents.

Data and code availability

- Data associated with this study is freely accessible via DOI: 10.5281/zenodo.7082978.
- All original code has been deposited at GitHub and is publicly available as of the date of publication. URL is listed in the key resources table.
- Any additional information required to reanalyse the data reported in this paper is available from the lead contact upon request.

Experimental model and subject details

Cell lines

Female Chinese hamster ovary cells (CHO-K1) and DHFR-deficient CHO cells stably transfected with human CCR5 (CHO-CCR5) [24] were verified mycoplasma-free and maintained in complete (+ 10% FCS with 4mM L-glutamine, 100U/ml penicillin and 0.1mg/ml streptomycin) Dulbecco's Modified Eagle Medium (DMEM) or MEM-alpha medium, respectively.

Method details

Materials

Tissue culture reagents and plastics were purchased from Invitrogen Life Technologies, (Paisley, UK), and chemicals from Sigma-Aldrich Company Ltd (Poole, UK), unless otherwise indicated. CCL5 (RANTES) was purchased from PeproTech EC Ltd.

Transfection and generation of new cell line:

CHO-GFP-CCR5 cell lines were generated by transfecting CHO-K1 with a pCDNA3.1 Hygro-GFP-CCR5 [31] construct in the absence of a strong pre-promoter amplification region, using the TransIT-X2 transfection reagent from Mirus (MIR 6003). CCR5 expression was maintained by culturing cells in the presence of 400 µg/ml hygromycin and GFP-CCR5 expressing cells were isolated for single-cell cloning through the process of serial dilution cloning. In this process, single GFP-CCR5 positive cells were seeded individually in a 96-well plate and expanded by continuous culture in the

presence of hygromycin. Selection of specific populations based on their clonality and relatively low GFP signal intensity was aided through the characterisation of GFP expression using Flow cytometry (CytoFLEX LX, Beckman Coulter) against non-transfected CHO-K1 controls, as shown in Figure 3. Analysis of Flow cytometry results was performed using CytExpert (Beckman Coulter).

GFP-CCR5 CHO cell preparation for PaTCH microscopy:
GFP-CCR5 CHO cells from an 80% confluent well of a 6-well plate were detached in Trypsin-EDTA and seeded on 1.5 mm thick round coverslips at a dilution of 1:10 3 days prior to mounting. Cell samples were fixed with a solution of 3% formaldehyde in Phosphate Buffer Saline (PBS) for 20 mins at room temperature, before being extensively washed in PBS. Finally, coverslips were mounted in Mowiol [49].

Immunofluorescence staining of CHO-CCR5 cells for SIM:
CHO-CCR5 cells from an 80% confluent 10 cm dish detached in Trypsin-EDTA were seeded on 1.5 mm thick round coverslips two days prior to mounting. The culture medium was then replaced with Binding Medium (BM: RPMI 1640 without carbonate or glutamine, 0.2% (w/v) BSA, 10 mM HEPES adjusted to pH 7). For chemokine treatment, CCL5 was added to the BM before incubating coverslips at 37°C for 5 min at a saturating concentration of 100 nM [24,26,50–52]. Incubation was stopped by fixing samples as described above. For staining, free aldehyde groups were quenched with a 50 mM NH4Cl solution for 20 mins before saturation of non-specific binding in PBS with 1% FCS (PBS/FCS). Cells on coverslips were labeled intact with DyLight 650-MC-5 (2 µg/ml) in PBS/FCS for an hour before washing in PBS and mounting samples in Mowiol, as described above. MC-5 is an anti-human CCR5 mAb grown from a hybridoma and purified by Prof. Matthias Mack [25]. MC-5 non-interference with CCL5 binding, CCR5 conformation, activation and internalisation has been validated by numerous studies [24,25,53] and has been previously used to follow chemokine-mediated CCR5 stimulation using TIRF [45]. MC-5 was fluorescently labeled using DyLight 650 NHS ester coupling kit (Thermo Fisher) with a dye:protein coupling ratio of 1.57:1.

PaTCH imaging

The Slimfield microscope (without alteration for PaTCH acquisition) is based on a custom-built epifluorescence/TIRF optical pathway [37,54,55]. An optimised angle of excitation beam delivery distinguishes PaTCH imaging from the traditionally used TIRF and HILO microscope settings, thereby facilitating the imaging of transmembrane proteins in mammalian cells [35]. In this study the angle of incidence of the excitation beam was set to a sub-critical angle of 55° by translation of a telescope lens, as calibrated using the lateral displacement of the beam downstream of the focal plane [56]. At this angle, we estimated that ~30% of the incident light is coupled into a reflected TIRF mode, with the associated enhancement of the excitation field at the surface. The remaining light couples into transmitted HILO modes, which extend the excitation field into regions of the basal membrane not directly contacting the coverslip, but not the interior of the cell.

The 488 nm wavelength laser (Coherent OBIS LX) was spatially filtered to the TEM_{00} mode and delivered by an oil-immersion objective lens (Nikon ApoTIRF, 100x, NA 1.49). The illumination covered an area c. 60 µm wide (diameter at $1/e^2$ peak intensity) in the sample plane as characterised using a sample of immobilised standard fluorescent microbeads (Promega). The source power was 30 mW, corresponding to an excitation intensity of approximately 0.5 kW/cm² at the sample.

A single image sequence was captured for each field of view in OME TIFF format using a Prime 95b camera (Teledyne Photometrics). The exposure time was 10 ms per frame, during which the laser was digitally triggered, and a total framerate of 77 fps over 1000 - 3000 frames at 53 nm/pixel magnification. The estimated lateral resolution is 180 nm, while the localization precision of each focus is approximately 40 nm [57]. The detection performance was characterised using *in vitro* recombinant GFP immobilised to a coverslip [36,58,59].

Single particle tracking

The custom software suite, ADEMScode (MATLAB, MathWorks) [60] was employed to detect local maxima inside circles of 8-pixel radius (foci), above background (averaged over 17 pixel squares) in each frame of a given image sequence. These foci were then thresholded using signal-to-noise ratio and were fitted with a Gaussian intensity mask to establish the super-resolved centroid, width and integrated intensity (background subtracted sum of pixel values). The foci were then linked into tracks based on their persistent overlap (75-100%) and intensity ratio (50-200%) across adjacent frames. A representative example of these super-resolved tracks overlaid on the parent PaTCH image is shown in Figure S3 a. The initial intensity of each track was linearly extrapolated back across the first five frames to the time point of initial laser exposure. This initial intensity was divided by the characteristic integrated intensity of a focus containing a single GFP in order to determine the number of GFP molecules present in each track, which, given the 1:1 labeling of the protein of interest, was equated with the CCR5 stoichiometry. Only tracks determined in the first 10 frames of laser exposure were then used for estimates of stoichiometry to avoid undercounting due to photobleaching. The characteristic brightness of a single GFP was estimated from the modal brightness of GFP-CCR5 foci after sufficient photobleaching, to ensure the presence of single GFP molecules. This value of brightness was confirmed to be broadly consistent with values gained from recombinant GFP immobilised to a coverslip as well as estimates of the GFP brightness determined from the monomeric intervals in intensity due to stepwise photobleaching of GFP-CCR5 foci, as identified by a Chung–Kennedy edge-preserving filter [61–64]. Representative examples of single molecule intensity traces towards the end of the photobleaching process are shown in Figure S3 b, with an inset trace demonstrating the accuracy of the estimation of the brightness of a single GFP probe. The collated stoichiometries of all tracks were represented as kernel density estimates with kernel width of 0.6 molecules, corresponding to the root mean squared (rms) detection sensitivity of the integrated intensity of a single GFP molecule in a focus (Figure 5). The periodicity was calculated by sorting the stoichiometries of a population of tracks [33] and taking the nearest-neighbour differences [62]. These intervals were themselves then plotted as a kernel density estimate with kernel width of 0.6 molecules. The periodicity was quoted as the

modal peak in this distribution (Figure 5 inset), with the error estimated as 0.6 molecules, multiplied by the square root of the ratio of the mean stoichiometry and the number of extrapolation points, divided by the number of tracks under the main peak.

SIM imaging

Super-resolution imaging was performed using a custom SIM system built around an inverted widefield epifluorescence microscope [65,66]. Illumination patterns were generated by projecting the spatially filtered image of a binary phase grating, displayed on a liquid-crystal-on-silicon spatial light modulator (SLM) (SXGA-3DM, Forth Dimension Displays), into the sample. Images were recorded using a scientific CMOS camera (Flash 4.0, Hamamatsu Photonics), with the global exposure period of the camera's rolling shutter synchronised to the SLM. Each super-resolution image was reconstructed from nine raw images captured under illumination of the sample with a series of sinusoidal excitation patterns (three pattern orientations separated by 120° and pattern phases separated by $2\pi/3$ per orientation). High pass filtering was applied to suppress out-of-focus information close to the centre of each separated Fourier space information passband [65]. Passbands were then shifted to their origins in Fourier space, corrected for phase offsets determined by complex linear regression in the overlap regions, and combined through a Wiener filter [67]. Images of Dylight 650-MC-5 labeled CHO-CCR5 were acquired using a quad band fluorescence filter cube (TRF89901-EM, Chroma) and a 60x/1.3 silicone immersion objective lens (UPLSAPO, Olympus) with excitation at 638 nm using a diode laser (Luxx, Omicron), with an effective lateral (Abbe) resolution of approximately 170 nm. Post reconstruction, images captured at different focal offsets were corrected for photobleaching by scaling using an exponential decay curve measured by repeated imaging of the same region of a cell under identical conditions.

Clustering analysis

Images of CHO-CCR5 labeled with DyLight 650-MC-5 obtained using SIM underwent cell boundary segmentation to remove extracellular foci. Images then underwent binarization using a combination (in parallel, followed by an AND operation) of global Otsu thresholding and local Otsu thresholding with a rolling ball radius of 25 pixels. The binary images revealed objects corresponding to local enrichment of CCR5. The number of objects, and the characteristic properties of each object, including area, centroid and circularity were determined using the *Analyze Objects* function in ImageJ/Fiji. The number density of objects (Figure 2 d) was calculated using a 2D kernel density estimate of the object centroid coordinates, with kernel width of the widefield lateral resolution, ~180 nm.

Centroid coordinates of foci were analysed using ClusDoc software [68]. The relative clustering or dispersal of objects was assessed for each individual cell using the Ripley H function. The Ripley H function is equal to the Ripley L function less the radius, $H(r)=L(r)-r$, where $L(r)$ is the radius of a circle in which the experimentally counted points inside would otherwise be uniformly distributed [28]. Thus, Ripley H is a measure of the deviation from uniform distribution, $H(r)=0$, with positive deviations corresponding to "attractive" clustering of objects. The clustering results were validated against simulated negative and positive controls, which were point clouds

generated respectively from random 2D coordinates or points on a square lattice with rms noise of half the lattice spacing (MATLAB). Nearest neighbour distances were calculated using the minimum value of H(r) associated with the initial negative H(r) values, values were averaged over all cells to provide a mean value ± standard error of the mean. Clustering gradients were determined as the peak of a kernel density estimate of gradient values calculated pairwise between adjacent H(r), with a kernel width of 0.001.

Supplemental characterisations

To further characterise PaTCH microscopy, fixed samples of CHO-GFP-CCR5 were imaged using a varied angle of incidence of the excitation beam (see Figure S1). Individual cells underwent an epifluorescence prebleach lasting 750 frames (~10 s) to minimize the effect of photobleaching on the comparison of imaging modes. Cells were then imaged for 100 frames using angles of incidence of 45°, 55° and 62° sequentially, corresponding to HILO, PaTCH and TIRF microscopy respectively. Acquired image stacks formed maximum z intensity projections of singular cells under all imaging modes. Puncta were localized using intensity thresholding, allowing the spatial distributions of puncta within PaTCH images to be overlaid onto HILO and TIRF images, thereby facilitating the determination of puncta present across multiple imaging modes. The signal of isolated puncta and the adjacent background were determined under a circular window of 6 pixels in diameter. Signal and background intensities are represented as the raw integrated density, captured under the circular window, normalized to the global background of the sample. Global background was calculated as the average raw integrated density in the extracellular volume across the three imaging modes. Signal to background ratio averages were calculated using 10 puncta from each of the three imaging modes in order to provide a mean ± SEM.

Calcium flux assays were performed to confirm the functionality of GFP-CCR5 (see Figure S2 a). Cells were detached in PBS 10mM EDTA and washed twice in PBS without calcium before resuspension in PBS at 2 x 106 cells/ml. Quest Fluo-8 AM was added to give a 2.5 µM concentration and cells were incubated for 30 minutes in the dark at room temperature. Excess dye was removed using two PBS washes before cell resuspension at 1 x 106 cells in HBSS (1.26 mM CaCl2). A Cytoflex S flow cytometer employing a 488 nm argon laser (Beckman Coulter) was used to determine the changes in Intracellular calcium concentration within 500 µl aliquots of cells in response to 10 nM CCL5, the known optimal concentration for calcium flux assays [52]. Labelled aliquots were kept on ice until use, a portion of which were pre-exposed to 400 nM of the CCR5 antagonist TAK-779. Cell aliquots were aspirated before CCL5 was added in order to define the baseline fluorescence of the sample. Acquisition was resumed for the duration of the response and repeated, as required. A blank stimulation was used to control for the mechanical impact of instrument on readings. Collected data were analyzed by plotting the fluorescence signal (fluo-8-Ca2+-FITC) against time, with successive gates of 5 second intervals for the duration of the response. Results were reported as fluorescence normalized to the baseline signal of each sample before stimulation and graphs were plotted in Prism v9.4.1 (GraphPad Software Inc., La Jolla, USA).

Flow cytometry-based assays were performed to confirm the internalization of GFP-CCR5 upon extended exposure to the super-agonist PSC-RANTES (gifted by Prof. Oliver Hartley, University of Geneva) (see Figure S2 b). Assays were performed in binding medium (RPMI 1640 without bicarbonate, containing 0.2% BSA and 10 mM Hepes, pH 7.0). Cells were detached in PBS 10mM EDTA and resuspended at 2×10^6 cells/mL and incubated in binding medium alone or containing 100 nM PSC-RANTES for up to 1 hour at 37°C. Aliquots (100 µl) of suspended cells were taken for each time point and transferred to a 96W plate kept on ice. At the end of the time course, each sample was split between two wells for antibody labelling with 2D7, a CCR5-specific monoclonal antibody recognising the chemokine binding site, and with an anti-GFP monoclonal antibody in FACS Buffer (PBS, 1%FCS, Azide). Samples were fixed overnight in FACS buffer containing 1% formaldehyde. Bound antibodies were then detected using GAM-DyLight 650 in FACS Buffer, and all samples were analysed using a CytoFlex S flow cytometer (Beckman Coulter). For each antibody staining, the percentage of fluorescent signal was calculated from the specific mean fluorescence intensity (MFI= CCR5 antibody MFI subtracted for background).

Quantification and statistical analysis

MATLAB was used for statistical tests as reported in the Results section. To account for multiple comparisons (across ≤ 5 tests per sample: intensity/stoichiometry, periodicity and cluster density), we used a conservative Bonferroni-adjusted significance level of $α = 0.05/5 = 0.01$. Nonparametric statistical tests were used to test for significance, chiefly the Brunner-Menzel test with exact values of N and p reported. N represents in each case either the number of foci or the number of cells. An asterisk (*) indicates $p < 0.01$ via Brunner-Munzel test, i.e. stochastic inequality of the compared populations (see Figure 6).

As the underlying distributions and variances were unknown *a priori*, a target sample size of n ≥ 5 cells (and n ≥ 24 tracks) per condition was estimated. These targets were based on a minimum detection level of 1 s.d. at 80% power under normal statistics for a one-tailed or two-tailed Z-test respectively. Cell cultures were assigned randomly for ligand +/- groups. Of 24 total SIM (21 PaTCH) acquisitions, 23 (21) were included in analysis based on sufficient quality of the initial microscope focus. The lower target number of cells reflects the experimental throughput of the microscopy techniques.

Supplemental video titles and legends

Video S1. A 3D Video of a CHO-CCR5 cell shows distinct puncta throughout the membrane. Related to Figure 1. *3D reconstruction of 7 Individual SIM images of a CHO-CCR5 cell labeled with DyLight 650-MC-5, as shown in Figure 1 a-g). (Scale bar 2 µm).*

Video S2. A 3D Video of a CHO-CCR5 cell after ligation shows retention of distinct puncta throughout cell. Related to Figure 6. *3D reconstruction of 7*

Individual SIM images of a CHO-CCR5 cell labeled with DyLight 650-MC-5 and perturbed with CCL5, as shown in Figure 6 a-g). (Scale bar 2 µm).

References

1. Aldinucci, D., Borghese, C., and Casagrande, N. (2020). The ccl5/ccr5 axis in cancer progression. Cancers (Basel) *12*, 1–30. 10.3390/cancers12071765.

2. Upadhyaya, C., Jiao, X., Ashton, A., Patel, K., Kossenkov, A. v., and Pestell, R.G. (2020). The G protein coupled receptor CCR5 in cancer. In, pp. 29–47. 10.1016/bs.acr.2019.11.001.

3. Jiao, X., Nawab, O., Patel, T., Kossenkov, A. v., Halama, N., Jaeger, D., and Pestell, R.G. (2019). Recent advances targeting CCR5 for cancer and its role in immuno-oncology. Cancer Res *79*, 4801–4807. 10.1158/0008-5472.CAN-19-1167.

4. Aldinucci, D., and Colombatti, A. (2014). The inflammatory chemokine CCL5 and cancer progression. Mediators Inflamm *2014*. 10.1155/2014/292376.

5. Aldinucci, D., Borghese, C., and Casagrande, N. (2019). Formation of the Immunosuppressive Microenvironment of Classic Hodgkin Lymphoma and Therapeutic Approaches to Counter It. International Journal of Molecular Sciences 2019, Vol. 20, Page 2416 *20*, 2416. 10.3390/IJMS20102416.

6. Chang, L.Y., Lin, Y.C., Mahalingam, J., Huang, C.T., Chen, T.W., Kang, C.W., Peng, H.M., Chu, Y.Y., Chiang, J.M., Dutta, A., et al. (2012). Tumor-derived chemokine CCL5 enhances TGF-β-mediated killing of CD8 + T cells in colon cancer by T-regulatory cells. Cancer Res *72*, 1092–1102. 10.1158/0008-5472.CAN-11-2493.

7. Tan, M.C.B., Goedegebuure, P.S., Belt, B.A., Flaherty, B., Sankpal, N., Gillanders, W.E., Eberlein, T.J., Hsieh, C.-S., and Linehan, D.C. (2009). Disruption of CCR5-Dependent Homing of Regulatory T Cells Inhibits Tumor Growth in a Murine Model of Pancreatic Cancer. The Journal of Immunology *182*, 1746–1755. 10.4049/JIMMUNOL.182.3.1746.

8. Aldinucci, D., Lorenzon, D., Cattaruzza, L., Pinto, A., Gloghini, A., Carbone, A., and Colombatti, A. (2008). Expression of CCR5 receptors on Reed–Sternberg cells and Hodgkin lymphoma cell lines: Involvement of CCL5/Rantes in tumor cell growth and microenvironmental interactions. Int J Cancer *122*, 769–776. 10.1002/ijc.23119.

9. Aldinucci, D., and Casagrande, N. (2018). Inhibition of the CCL5/CCR5 Axis against the Progression of Gastric Cancer. International Journal of Molecular Sciences 2018, Vol. 19, Page 1477 *19*, 1477. 10.3390/IJMS19051477.

10. Vaday, G.G., Peehl, D.M., Kadam, P.A., and Lawrence, D.M. (2006). Expression of CCL5 (RANTES) and CCR5 in prostate cancer. Prostate *66*, 124–134. 10.1002/PROS.20306.

11. Miao, M., de Clercq, E., and Li, G. (2020). Clinical significance of chemokine receptor antagonists. Expert Opin Drug Metab Toxicol *16*, 11–30. 10.1080/17425255.2020.1711884.

12. Haag, G.M., Halama, N., Springfeld, C., Grün, B., Apostolidis, L., Zschaebitz, S., Dietrich, M., Berger, A.-K., Weber, T.F., Zoernig, I., et al. (2020). Combined PD-1 inhibition (Pembrolizumab) and CCR5 inhibition (Maraviroc) for the treatment of refractory microsatellite stable (MSS) metastatic colorectal cancer (mCRC): First results of the PICCASSO

phase I trial. Journal of Clinical Oncology *38*, 3010–3010. 10.1200/JCO.2020.38.15_SUPPL.3010.

13. Fox, J.M., Kasprowicz, R., Hartley, O., and Signoret, N. (2015). CCR5 susceptibility to ligand-mediated down-modulation differs between human T lymphocytes and myeloid cells. J Leukoc Biol *98*, 59–71. 10.1189/JLB.2A0414-193RR.

14. Colin, P., Bénureau, Y., Staropoli, I., Wang, Y., Gonzalez, N., Alcami, J., Hartley, O., Brelot, A., Arenzana-Seisdedos, F., and Lagane, B. (2013). HIV-1 exploits CCR5 conformational heterogeneity to escape inhibition by chemokines. Proc Natl Acad Sci U S A *110*, 9475–9480. 10.1073/pnas.1222205110.

15. Colin, P., Zhou, Z., Staropoli, I., Garcia-Perez, J., Gasser, R., Armani-Tourret, M., Benureau, Y., Gonzalez, N., Jin, J., Connell, B.J., et al. (2018). CCR5 structural plasticity shapes HIV-1 phenotypic properties. PLoS Pathog *14*, e1007432. 10.1371/JOURNAL.PPAT.1007432.

16. Weichseldorfer, M., Tagaya, Y., Reitz, M., DeVico, A.L., and Latinovic, O.S. (2022). Identifying CCR5 coreceptor populations permissive for HIV-1 entry and productive infection: implications for in vivo studies. J Transl Med *20*, 1–12. 10.1186/S12967-022-03243-8.

17. Jin, J., Momboisse, F., Boncompain, G., Koensgen, F., Zhou, Z., Cordeiro, N., Arenzana-Seisdedos, F., Perez, F., Lagane, B., Kellenberger, E., et al. (2018). CCR5 adopts three homodimeric conformations that control cell surface delivery. Sci Signal *11*, 2869. 10.1126/SCISIGNAL.AAL2869.

18. Martínez-Muñoz, L., Villares, R., Rodríguez-Fernández, J.L., Rodríguez-Frade, J.M., and Mellado, M. (2018). Remodeling our concept of chemokine receptor function: From monomers to oligomers. J Leukoc Biol *104*, 323–331. 10.1002/JLB.2MR1217-503R.

19. Berro, R., Klasse, P.J., Lascano, D., Flegler, A., Nagashima, K.A., Sanders, R.W., Sakmar, T.P., Hope, T.J., and Moore, J.P. (2011). Multiple CCR5 Conformations on the Cell Surface Are Used Differentially by Human Immunodeficiency Viruses Resistant or Sensitive to CCR5 Inhibitors. J Virol *85*, 8227–8240. 10.1128/jvi.00767-11.

20. Tian, H., Furstenberg, A., and Huber, T. (2017). Labeling and single-molecule methods to monitor G proteincoupled receptor dynamics. Chem Rev *117*, 186–245. 10.1021/ACS.CHEMREV.6B00084.

21. Kasai, R.S., and Kusumi, A. (2014). Single-molecule imaging revealed dynamic GPCR dimerization. Curr Opin Cell Biol *27*, 78–86. 10.1016/J.CEB.2013.11.008.

22. Joseph, M.D., Bort, E.T., Grose, R.P., McCormick, P.J., and Simoncelli, S. (2021). Quantitative Super-Resolution Imaging for the Analysis of GPCR Oligomerization. Biomolecules 2021, Vol. 11, Page 1503 *11*, 1503. 10.3390/BIOM11101503.

23. Signoret, N., Christophe, T., Oppermann, M., and Marsh, M. (2004). pH-Independent Endocytic Cycling of the Chemokine Receptor CCR5. Traffic *5*, 529–543. 10.1111/J.1600-0854.2004.00200.X.

24. Signoret, N., Hewlett, L., Wavre, S., Pelchen-Matthews, A., Oppermann, M., and Marsh, M. (2005). Agonist-induced endocytosis of CC chemokine receptor 5 is clathrin dependent. Mol Biol Cell *16*, 902–917. 10.1091/MBC.E04-08-0687.

25.   Signoret, N., Pelchen-Matthews, A., Mack, M., Proudfoot, A.E.I., and Marsh, M. (2000). Endocytosis and Recycling of the HIV Coreceptor Ccr5. Journal of Cell Biology *151*, 1281–1294. 10.1083/jcb.151.6.1281.

26.   Mack, M., Luckow, B., Nelson, P.J., Cihak, J., Simmons, G., Clapham, P.R., Signoret, N., Marsh, M., Stangassinger, M., Borlat, F., et al. (1998). Aminooxypentane-RANTES Induces CCR5 Internalization but Inhibits Recycling: A Novel Inhibitory Mechanism of HIV Infectivity. Journal of Experimental Medicine *187*, 1215–1224. 10.1084/JEM.187.8.1215.

27.   Tokunaga, M., Imamoto, N., and Sakata-Sogawa, K. (2008). Highly inclined thin illumination enables clear single-molecule imaging in cells. Nature Methods 2008 5:2 *5*, 159–161. 10.1038/nmeth1171.

28.   Kiskowski, M.A., Hancock, J.F., and Kenworthy, A.K. (2009). On the use of Ripley's K-function and its derivatives to analyze domain size. Biophys J *97*, 1095–1103. 10.1016/J.BPJ.2009.05.039.

29.   Jin, X., Lee, J.E., Schaefer, C., Luo, X., Wollman, A.J.M., Payne-Dwyer, A.L., Tian, T., Zhang, X., Chen, X., Li, Y., et al. (2021). Membraneless organelles formed by liquid-liquid phase separation increase bacterial fitness. Sci Adv *7*. 10.1126/SCIADV.ABH2929.

30.   Yuan, Y., Jacobs, C.A., Llorente Garcia, I., Pereira, P.M., Lawrence, S.P., Laine, R.F., Marsh, M., and Henriques, R. (2021). Single-Molecule Super-Resolution Imaging of T-Cell Plasma Membrane CD4 Redistribution upon HIV-1 Binding. Viruses *13*. 10.3390/V13010142.

31.   Gómez-Moutón, C., Lacalle, R.A., Mira, E., Jiménez-Baranda, S., Barber, D.F., Carrera, A.C., Martínez-A., C., and Mañes, S. (2004). Dynamic redistribution of raft domains as an organizing platform for signaling during cell chemotaxis. Journal of Cell Biology *164*, 759–768. 10.1083/jcb.200309101.

32.   Leake, M.C. (2014). Analytical tools for single-molecule fluorescence imaging in cellulo. Phys. Chem. Chem. Phys. *16*, 12635–12647. 10.1039/C4CP00219A.

33.   Wollman, A.J.M., Shashkova, S., Hedlund, E.G., Friemann, R., Hohmann, S., and Leake, M.C. (2017). Transcription factor clusters regulate genes in eukaryotic cells. Elife *6*. 10.7554/ELIFE.27451.

34.   Escola, J.-M., Kuenzi, G., Gaertner, H., Foti, M., and Hartley, O. (2010). CC Chemokine Receptor 5 (CCR5) Desensitization. Journal of Biological Chemistry *285*, 41772–41780. 10.1074/jbc.M110.153460.

35.   Wollman, A., Fournier, C., Llorente-Garcia, I., Harriman, O., Payne-Dwyer, A., Shashkova, S., Zhou, P., Liu, T.-C., Ouaret, D., Wilding, J., et al. (2022). Critical roles for EGFR and EGFR-HER2 clusters in EGF binding of SW620 human carcinoma cells. J R Soc Interface *19*. 10.1098/rsif.2022.0088.

36.   Leake, M.C., Chandler, J.H., Wadhams, G.H., Bai, F., Berry, R.M., and Armitage, J.P. (2006). Stoichiometry and turnover in single, functioning membrane protein complexes. Nature *443*, 355–358. 10.1038/nature05135.

37.   Syeda, A.H., Wollman, A.J.M., Hargreaves, A.L., Howard, J.A.L., Bruning, J.G., McGlynn, P., and Leake, M.C. (2019). Single-molecule live cell imaging of Rep reveals the dynamic interplay

between an accessory replicative helicase and the replisome. Nucleic Acids Res *47*, 6287. 10.1093/NAR/GKZ298.

38. Wollman, A.J.M., Muchová, K., Chromiková, Z., Wilkinson, A.J., Barák, I., and Leake, M.C. (2020). Single-molecule optical microscopy of protein dynamics and computational analysis of images to determine cell structure development in differentiating Bacillus subtilis. Comput Struct Biotechnol J *18*, 1474–1486. 10.1016/J.CSBJ.2020.06.005.

39. Leake, M.C., Greene, N.P., Godun, R.M., Granjon, T., Buchanan, G., Chen, S., Berry, R.M., Palmer, T., and Berks, B.C. (2008). Variable stoichiometry of the TatA component of the twin-arginine protein transport system observed by in vivo single-molecule imaging. Proceedings of the National Academy of Sciences *105*, 15376–15381. 10.1073/pnas.0806338105.

40. Reyes-Lamothe, R., Sherratt, D.J., and Leake, M.C. (2010). Stoichiometry and Architecture of Active DNA Replication Machinery in Escherichia coli. Science (1979) *328*, 498–501. 10.1126/science.1185757.

41. Li, J., Ding, Y., Liu, H., He, H., Yu, D., Wang, X., Wang, X., Yu, X., Ge, B., and Huang, F. (2021). Oligomerization-Enhanced Receptor-Ligand Binding Revealed by Dual-Color Simultaneous Tracking on Living Cell Membranes. Journal of Physical Chemistry Letters *12*, 8164–8169. 10.1021/ACS.JPCLETT.1C01844.

42. Delhaye, M., Gravot, A., Ayinde, D., Niedergang, F., Alizon, M., and Brelot, A. (2007). Identification of a Postendocytic Sorting Sequence in CCR5. Mol Pharmacol *72*, 1497–1507. 10.1124/MOL.107.038422.

43. Hammad, M.M., Kuang, Y.Q., Yan, R., Allen, H., and Dupre, D.J. (2010). Na+/H+ Exchanger Regulatory Factor-1 Is Involved in Chemokine Receptor Homodimer CCR5 Internalization and Signal Transduction but Does Not Affect CXCR4 Homodimer or CXCR4-CCR5 Heterodimer. Journal of Biological Chemistry *285*, 34653–34664. 10.1074/JBC.M110.106591.

44. Mueller, A., Kelly, E., and Strange, P.G. (2002). Pathways for internalization and recycling of the chemokine receptor CCR5. Blood *99*, 785–791. 10.1182/BLOOD.V99.3.785.

45. Grove, J., Metcalf, D.J., Knight, A.E., Wavre-Shapton, S.T., Sun, T., Protonotarios, E.D., Griffin, L.D., Lippincott-Schwartz, J., and Marsh, M. (2014). Flat clathrin lattices: stable features of the plasma membrane. Mol Biol Cell *25*, 3581–3594. 10.1091/mbc.e14-06-1154.

46. Martínez-Muñoz, L., Rodríguez-Frade, J.M., Barroso, R., Sorzano, C.Ó.S., Torreño-Pina, J.A., Santiago, C.A., Manzo, C., Lucas, P., García-Cuesta, E.M., Gutierrez, E., et al. (2018). Separating Actin-Dependent Chemokine Receptor Nanoclustering from Dimerization Indicates a Role for Clustering in CXCR4 Signaling and Function. Mol Cell *70*, 106-119.e10. 10.1016/J.MOLCEL.2018.02.034.

47. Ponjavic, A., McColl, J., Carr, A.R., Santos, A.M., Kulenkampff, K., Lippert, A., Davis, S.J., Klenerman, D., and Lee, S.F. (2018). Single-Molecule Light-Sheet Imaging of Suspended T Cells. Biophys J *114*, 2200–2211. 10.1016/j.bpj.2018.02.044.

48. Sims, R.R., Abdul Rehman, S., Lenz, M.O., Benaissa, S.I., Bruggeman, E., Clark, A., Sanders, E.W., Ponjavic, A., Muresan, L., Lee, S.F., et al. (2020). Single molecule light field microscopy. Optica *7*, 1065. 10.1364/OPTICA.397172.

49.   Kasprowicz, R., Rand, E., O'Toole, P.J., and Signoret, N. (2018). A correlative and quantitative imaging approach enabling characterization of primary cell-cell communication: Case of human CD4+ T cell-macrophage immunological synapses. Scientific Reports 2018 8:1 *8*, 1–17. 10.1038/s41598-018-26172-3.

50.   Proudfoot, A.E.I., Handel, T.M., Johnson, Z., Lau, E.K., LiWang, P., Clark-Lewis, I., Borlat, F., Wells, T.N.C., and Kosco-Vilbois, M.H. (2003). Glycosaminoglycan binding and oligomerization are essential for the *in vivo* activity of certain chemokines. Proceedings of the National Academy of Sciences *100*, 1885–1890. 10.1073/pnas.0334864100.

51.   Andrews, G., Jones, C., and Wreggett, K.A. (2008). An Intracellular Allosteric Site for a Specific Class of Antagonists of the CC Chemokine G Protein-Coupled Receptors CCR4 and CCR5. Mol Pharmacol *73*, 855–867. 10.1124/mol.107.039321.

52.   Combadiere, C., Ahuja, S.K., Lee Tiffany, H., and Murphy, P.M. (1996). Cloning and functional expression of CC CKR5, a human monocyte CC chemokine receptor selective for MIP-1α, MIP-1β, and RANTES. J Leukoc Biol *60*, 147–152. 10.1002/jlb.60.1.147.

53.   Blanpain, C., Vanderwinden, J.-M., Cihak, J., Wittamer, V., le Poul, E., Issafras, H., Stangassinger, M., Vassart, G., Marullo, S., Schlo÷ndorff, D., et al. (2002). Multiple Active States and Oligomerization of CCR5 Revealed by Functional Properties of Monoclonal Antibodies. Mol Biol Cell *13*, 723–737. 10.1091/mbc.01-03-0129.

54.   Plank, M., Wadhams, G.H., and Leake, M.C. (2009). Millisecond timescale slimfield imaging and automated quantification of single fluorescent protein molecules for use in probing complex biological processes. Integrative Biology *1*, 602. 10.1039/b907837a.

55.   Payne-Dwyer, A., and Leake, M. (2022). Single-molecular quantification of flowering control proteins within nuclear condensates in live whole Arabidopsis root. In M.C. (eds) Chromosome Architecture. Methods in Molecular Biology, pp. 311–328. 10.1007/978-1-0716-2221-6_21.

56.   Dresser, L., Hunter, P., Yendybayeva, F., Hargreaves, A.L., Howard, J.A.L., Evans, G.J.O., Leake, M.C., and Quinn, S.D. (2021). Amyloid-β oligomerization monitored by single-molecule stepwise photobleaching. Methods *193*, 80–95. 10.1016/J.YMETH.2020.06.007.

57.   Lenn, T., and Leake, M.C. (2012). Experimental approaches for addressing fundamental biological questions in living, functioning cells with single molecule precision. Open Biol *2*. 10.1098/RSOB.120090.

58.   Delalez, N.J., Wadhams, G.H., Rosser, G., Xue, Q., Brown, M.T., Dobbie, I.M., Berry, R.M., Leake, M.C., and Armitage, J.P. (2010). Signal-dependent turnover of the bacterial flagellar switch protein FliM. Proceedings of the National Academy of Sciences *107*, 11347–11351. 10.1073/pnas.1000284107.

59.   Wollman, A.J.M., Hedlund, E.G., Shashkova, S., and Leake, M.C. (2020). Towards mapping the 3D genome through high speed single-molecule tracking of functional transcription factors in single living cells. Methods *170*, 82–89. 10.1016/J.YMETH.2019.06.021.

60.   Miller, H., Zhou, Z., Wollman, A.J.M., and Leake, M.C. (2015). Superresolution imaging of single DNA molecules using stochastic photoblinking of minor groove and intercalating dyes. Methods *88*, 81–88. 10.1016/j.ymeth.2015.01.010.

61.   Wollman, A.J.M., and Leake, M.C. (2015). Millisecond single-molecule localization microscopy combined with convolution analysis and automated image segmentation to determine protein concentrations in complexly structured, functional cells, one cell at a time. Faraday Discuss *184*, 401–424. 10.1039/C5FD00077G.

62.   Payne-Dwyer, A.L., Syeda, A.H., Shepherd, J.W., Frame, L., and Leake, M.C. (2022). RecA and RecB: probing complexes of DNA repair proteins with mitomycin C in live *Escherichia coli* with single-molecule sensitivity. J R Soc Interface *19*. 10.1098/rsif.2022.0437.

63.   Leake, M.C., Wilson, D., Gautel, M., and Simmons, R.M. (2004). The Elasticity of Single Titin Molecules Using a Two-Bead Optical Tweezers Assay. Biophys J *87*, 1112–1135. 10.1529/biophysj.103.033571.

64.   Leake, M.C., Wilson, D., Bullard, B., and Simmons, R.M. (2003). The elasticity of single kettin molecules using a two-bead laser-tweezers assay. FEBS Lett *535*, 55–60. 10.1016/S0014-5793(02)03857-7.

65.   O'Holleran, K., and Shaw, M. (2014). Optimized approaches for optical sectioning and resolution enhancement in 2D structured illumination microscopy. Biomedical Optics Express, Vol. 5, Issue 8, pp. 2580-2590 *5*, 2580–2590. 10.1364/BOE.5.002580.

66.   Shaw, M., Zajiczek, L., and O'Holleran, K. (2015). High speed structured illumination microscopy in optically thick samples. Methods *88*, 11–19. 10.1016/J.YMETH.2015.03.020.

67.   Gustafsson, M.G.L., Shao, L., Carlton, P.M., Wang, C.J.R., Golubovskaya, I.N., Cande, W.Z., Agard, D.A., and Sedat, J.W. (2008). Three-dimensional resolution doubling in wide-field fluorescence microscopy by structured illumination. Biophys J *94*, 4957–4970. 10.1529/BIOPHYSJ.107.120345.

68.   Pageon, S. v., Nicovich, P.R., Mollazade, M., Tabarin, T., and Gaus, K. (2016). Clus-DoC: a combined cluster detection and colocalization analysis for single-molecule localization microscopy data. Mol Biol Cell *27*, 3627–3636. 10.1091/mbc.e16-07-0478.
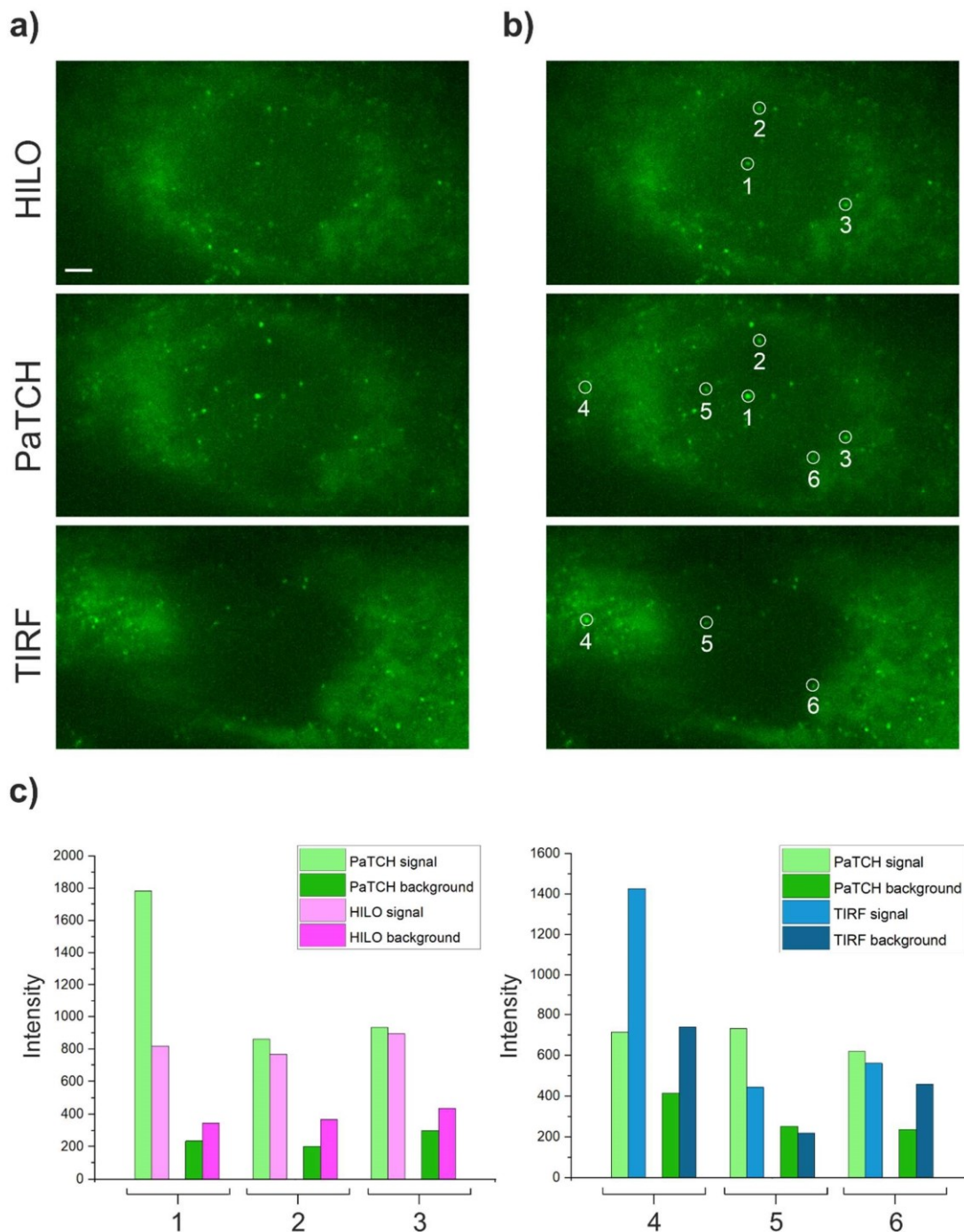
Figure S1. Comparison of HILO, PaTCH and TIRF imaging modes for the single molecule detection of GFP-CCR5 in CHO-GFP-CCR5. Related to Figure 4. a) GFP-CCR5 expressing CHO cell imaged using HILO, PaTCH and TIRF microscopy. Thereby revealing the increased signal of puncta within the basal membrane in PaTCH when compared with HILO, whilst demonstrating the uniformity of excitation of the basal membrane in PaTCH when compared with TIRF. (Scale bar 2 μm). b) Circular overlays highlighting CCR5 assemblies present in both HILO/PaTCH images and in both TIRF/PaTCH images. Overlays are numbered to facilitate further analysis. c) Comparison of signal and background between HILO and PaTCH imaging modes, in puncta labelled 1-3, and between TIRF and PaTCH imaging modes, in puncta labelled 4-6. Intensity represents the raw integrated density,

captured using a 6-pixel diameter circle, above a mean global background calculated using the extracellular space. Measurements of signal were taken directly over the puncta, while measurements of local background were taken adjacent to puncta. In general, puncta imaged using PaTCH benefit from a signal enhancement, relative to HILO, due to the TIRF-coupled component of illumination. Further, although TIRF is capable of providing enhanced signal relative to PaTCH, as seen in puncta 4, this restricted illumination mode results in higher background from fluorescent material close to the coverslip as well as lower signal from puncta not in close contact with the coverslip. These results combined with the result for the average signal to background ratio of 1.8 ± 0.1, 3.6 ± 0.6 and 2.4 ± 0.4 for puncta within HILO, PaTCH and TIRF respectively demonstrate the general increase in signal and reduction in background found in PaTCH when compared with HILO and TIRF.
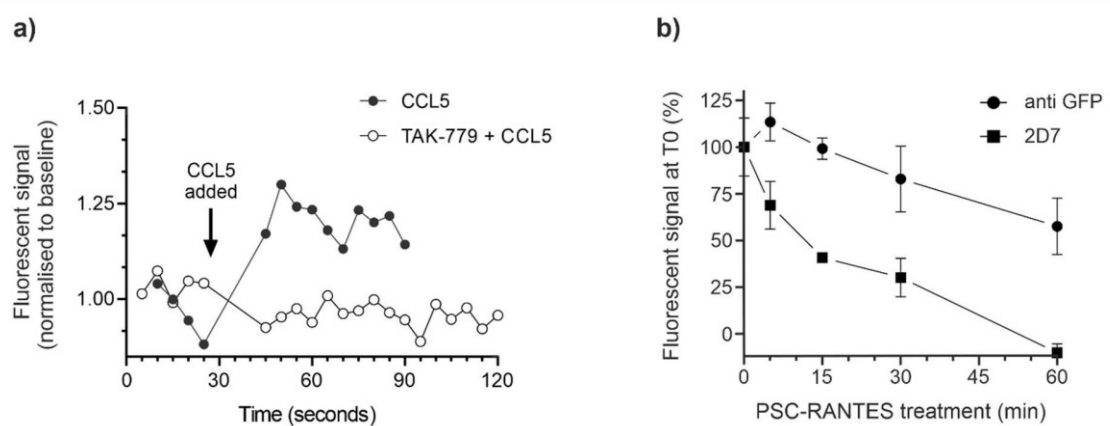

Figure S2. Increase in calcium flux, coupled with a decrease in anti GFP and 2D7 antibody binding, upon ligand stimulation confirms the functionality of GFP-CCR5. Related to Figure 3 and Figure 6. a) Calcium flux assay in which the change in calcium associated fluorescent signal is monitored within samples of CHO-GFP-CCR5 during live exposure to 10 nM CCL5, with and without pre-exposure to the CCR5 antagonist TAK-779. Thereby revealing an increase in CCL5-associated calcium signalling in the absence of an antagonist, suggesting a functional response of GFP-CCR5 to CCL5. Values of fluorescent signal are reported normalised to the average baseline fluorescence prior to CCL5 exposure. b) Fluorescent signals associated with antibodies bound to GFP (anti GFP) and the CCR5 chemokine binding site (2D7) are measured within CHO-GFP-CCR5 cells that underwent fixation after varying levels of exposure to the super-agonist PSC-RANTES at a concentration of 100 nM. Thereby revealing a decrease in both the accessibility of the GFP epitope and the availability of the chemokine binding site, suggesting the binding of ligand and the subsequent internalisation of GFPCCR5. Experiment was performed in triplicate and data are expressed as the mean values ± SEM.
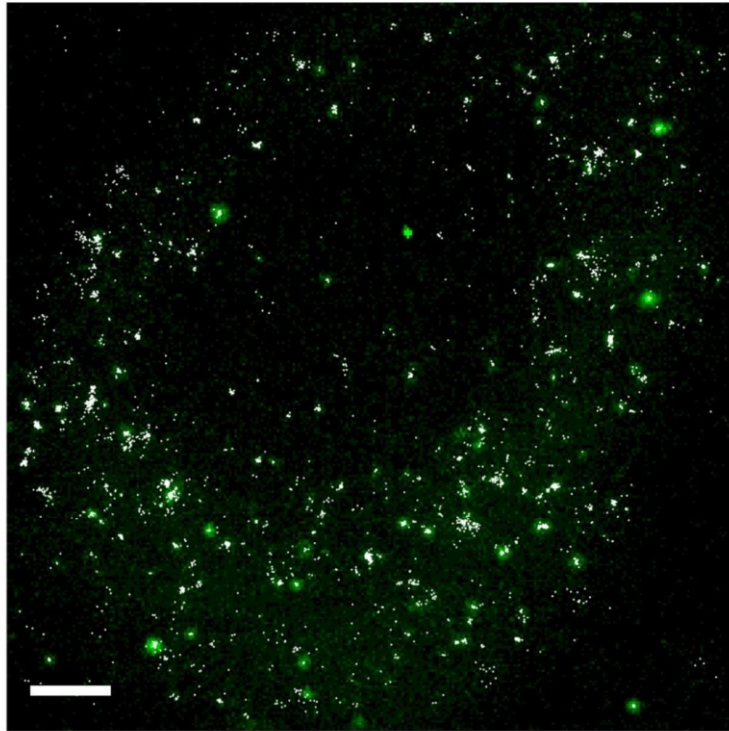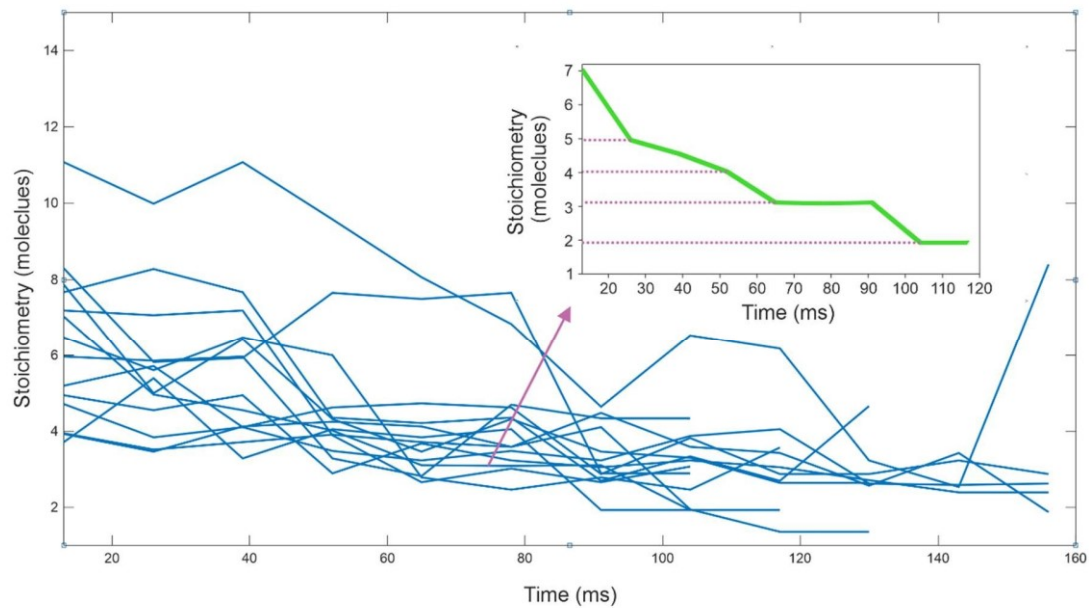
Figure S3. ADEMScode is used to detect foci within PaTCH microscopy images. Related to Figure 5. a) GFP-CCR5 expressing CHO cell imaged using PaTCH microscopy with an overlay(white) showing tracks determined by ADEMScode tracking (MATLAB). (Scale bar 2 μm). b) Chung–Kennedy edge-preserving filtered Intensity time traces revealing the photobleaching-induced intensity decay of tracked foci towards the end of the photobleaching process. The representative traces shown here exhibit fluctuations in intensity, however this effect is accounted for in the determination of stoichiometry. Inset trace (green) shows an example of a focus whose intensity underwent decay with minimal fluctuation, dropping in a stepwise fashion from an apparent

stoichiometry of 7 to 2, thereby supporting the accuracy of the estimated brightness of a single GFP molecule acquired from the modal brightness of monomeric GFP-CCR5.
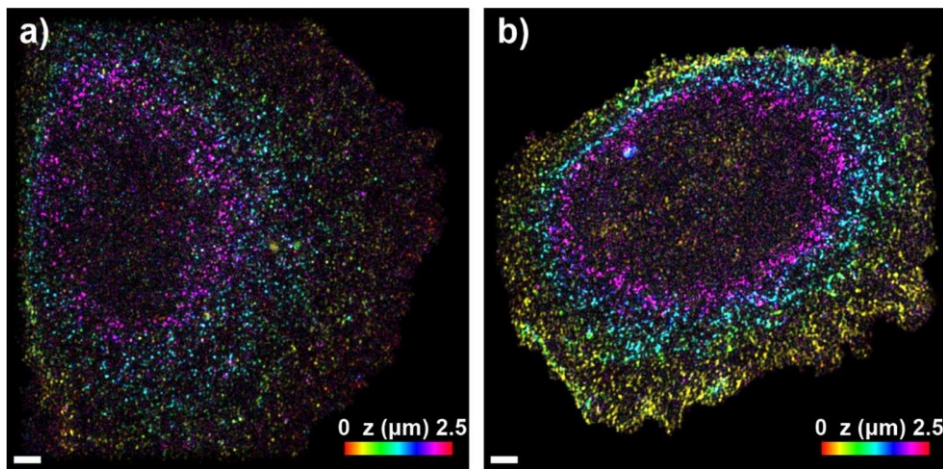

Figure S4. Comparison of cellular imaging demonstrates slight variation in brightness. Related to Figure 6. Color depth projection of cell images shown in a) Figure 1 h) and b) Figure 6 h). Comparison of which at identical contrast settings demonstrates the slight variation in brightness that can exist between cells. This change in brightness can stem from many factors, including the natural variance of expression in this non-clonal cell model. (Scale bar 2 μm).
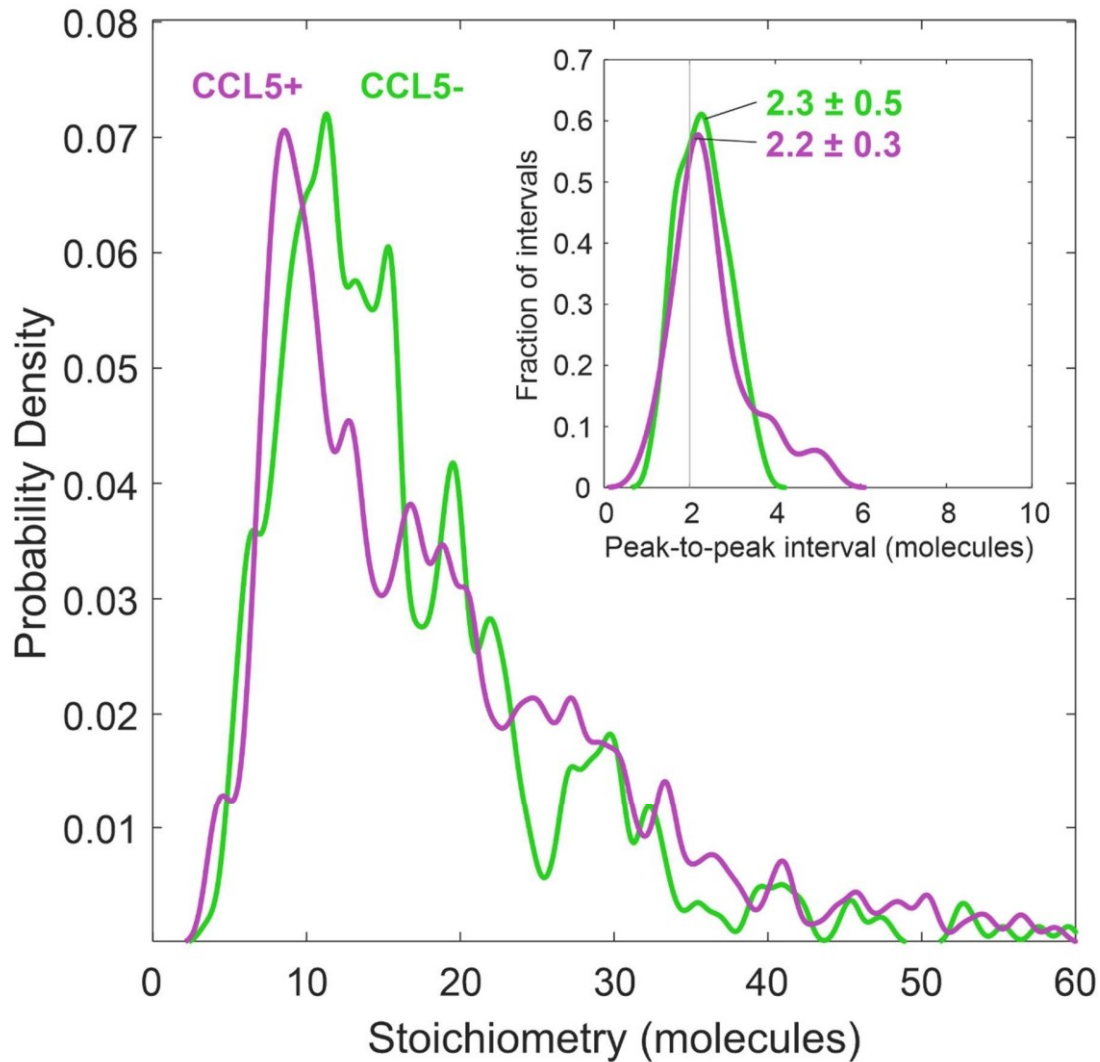
Figure S5. Periodic stoichiometry distribution indicates that CCR5 assemblies comprise dimeric subunits both before and after CCL5 exposure. Related to Figure 6. Kernel density estimates of stoichiometry and (inset) periodic stoichiometry intervals of GFP-CCR5 associated foci before (green) and after (magenta) the addition of CCL5 (N=460 or 507 tracks respectively) detected by PaTCH microscopy in GFP-CCR5 transfected CHO cells (N=9 and 11 cells respectively). Kernel width = 0.6 molecules, corresponding to the total uncertainty in the single molecule stoichiometry, rather than statistical fluctuations. Measured intervals in probability density or stoichiometry are therefore more reliable at lower stoichiometry. (BM test for difference in periodicity, p=0.479|* NS).